

# Microstructure, Micro-inclusions and Mineralogy along the EGRIP ice core - Part 2: Implications for paleo-mineralogy

Nicolas Stoll<sup>1</sup>, Maria Hörhold<sup>1</sup>, Tobias Erhardt<sup>1, 2</sup>, Jan Eichler<sup>1</sup>, Camilla Jensen<sup>2</sup>, and Ilka Weikusat<sup>1, 3</sup>

<sup>1</sup>Alfred Wegener Institute Helmholtz Centre for Polar and Marine Research, Bremerhaven, Germany

<sup>2</sup>Climate and Environmental Physics, Physics Institute and Oeschger Centre for Climate Change Research, University of Bern, Bern, Switzerland

<sup>3</sup>Department of Geosciences, Eberhard Karls University, Tübingen, Germany

**Correspondence:** Nicolas Stoll (nicolas.stoll@awi.de)

**Abstract.** Impurities in polar ice do not only allow the reconstruction of past atmospheric aerosol concentrationconcentrations, but also influence the physical properties of the ice. However, the mineralogy and location of impurities in ice and the involved processes are poorly understoodlocalisation of impurities inside the microstructure is still under debate and little is known about the mineralogy of solid inclusions. In particular, the general mineralogical diversity throughout an ice core and the specific distribution inside

5 the microstructure is poorly investigated, the impact of the mineralogy on the localisation of inclusions and other processes is thus hardly known. We use Continuous Flow Analysis to derive the dust particle concentrationand, optical microscopy and Cryo-Raman

spectroscopy to systematically locate and analyse the mineralogy of micro-inclusions in situ inside eleven solid ice samples from the upper 1340 m of the East Greenland Ice Core Project ice core. Micro-inclusions are more variable in mineralogy than previously observed and are mainly composed of mineral dust (quartz, mica and feldspar) and sulphates (mainly gypsum).

10 Inclusions of the same composition tend to cluster, but clustering frequency and mineralogy changes considerably with depth. A variety of sulphates dominate the upper 900 m while gypsum is the only sulphate in deeper samples, which however contain more mineral dust, nitrates and dolomite. The analysed part of the core can thus be divided into two depth regimes of different mineralogy, and to a lesser degree of spatial distribution, which could originate from different chemical reactions in the ice or

15 large-scale changes of ice cover in NE-Greenland during the Mid-Holocene. The complexity of impurity mineralogy on the metre- and centimetre-scale in polar ice is still underestimated and new methodological approaches are necessary to establish a comprehensive understanding of the role of impurities. Our results show that by applying new methods the mineralogy in ice cores, its complexity and importance for localisation studies, opens new avenues for understanding the role of impurities in ice cores.

## 1 Introduction

20 Deep ice cores from the polar ice sheets are a valuable archive of information: studying ice crystals allows the analysis of ice dynamics (e.g., Thorsteinsson et al., 1997; Faria et al., 2014; Fitzpatrick et al., 2014) while impurities and isotopes preserved in the ice enable the reconstruction of the paleoclimate of our planet (e.g., Dahl-Jensen et al., 2013; EPICA Community Members, 2004). Soluble impurities Impurities form solid micro-inclusions or dissolve in the ice lattice or in grain and subgrain boundaries

as snow eventually transforms into ice. Soluble impurities (in water or ice) are chemical compounds, such as  $Na^+$ ,  $Cl^-$ , and  $NO_3^-$ , and chemical compounds of atmospheric, marine, terrestrial or biological origin which dissolve dissolving in the lattice (Legrand and Delmas, 1988). They can also originate from salts dissociated into ions (Legrand and Mayewski, 1997; Della Lunga et al., 2014) or from dissolved gases such as hydrogen peroxide ( $H_2O_2$ ). Insoluble (Legrand and Mayewski, 1997). Water-insoluble impurities are rejected from the ice lattice, because they consist of lattice-incoherent phases (Ashby, 1969; Alley et al., 1986). They (Ashby, 1969; Alley et al., 1986) and range in size from sub-micrometre to hundreds of micrometres (Steffensen, 1997; Wegner et al., 2015; Simonsen et al., 2019). Micro-metre sized inclusions are called "micro-inclusions" and the focus of this study. Insoluble Water-insoluble impurities normally originate from terrestrial sources and mainly consist of salts (e.g., sulphates and nitrates) and mineral dust which is abundant in elements from the crust, such as Si, Al, Ca, and Fe, and in chemical compounds, such as  $FeSiO_3$ ,  $CaSiO_3$ , FeS, and  $SiO_2$  or  $Fe_2O_3$ .

Impurities have different transport histories and originate from different atmospheric aerosols, in the form of e.g., salt particles or terrestrial dust (Legrand and Mayewski, 1997; Weiss et al., 2002), and are deposited on ice sheets. They form solid micro-inclusions or dissolve in the ice lattice or in grain and subgrain boundaries as snow eventually transforms into ice. With time ice, and the impurities within, move into deeper parts of the ice column. Though the absolute concentrations are extremely low, the impurities inside the polar ice sheets are of interest for various research fields and applications. Tephra and sulphate layer are used for absolute dating and the layers provide a record of local and distal volcanic eruptions and offer a chronological correlation between ice cores. The sulphate record can provide time lines and information about the atmospheric impact of volcanic eruptions. Furthermore, the isotopic and chemical composition of impurities enable enables the investigation of climatic and atmospheric processes of the past.

Impurities in polar ice exist as soluble (in water or ice) or insoluble inclusions (e.g., dust particles, salts or droplets) and can be measured with a variety of methods, each with certain limitations. Main differences are the state of the analysed particles (soluble or insoluble in water or ice) and the applied aggregate phase of the sample: methods analysing a liquid and thus melting the ice are e.g., Ion Chromatography (IC) (Cole-Dai et al., 2006), CFA Continous Flow Analysis (CFA) (Röthlisberger et al., 2000a), and Inductively Coupled Plasma Mass Spectrometry (McConnell et al., 2002; Erhardt et al., 2019) while Laser Ablation Inductively Coupled Plasma Mass Spectrometry (LA-ICP-MS) (Reinhardt et al., 2001) and Cryo-Raman spectroscopy (Fukazawa et al., 1998) analyse solid ice samples.

The impurity content plays a major role regarding the physical properties of snow, firn, and ice, such as electrical conductivity (Alley and Woods, 1996; Wolff et al., 1997), permittivity (Wilhelms et al., 1998), and mechanical properties (e.g., Jones and Glen, 1969; Dahl-Jensen and Gundestrup, 1987; Paterson, 1991; Hörhold et al., 2012). Another important area is the impact of impurities on the deformation of ice (e.g., Jones and Glen, 1969; Petit et al., 1987; Iliescu and Baker, 2008; Eichler et al., 2019), which in turn influences the flow of ice - a major uncertainty regarding future projections of ice sheet behaviour and solid ice discharge. This chain of processes at the micro-scale resulting eventually in the large-scale deformation behaviour of ice needs to be better understood, especially in fast flowing ice, as present in ice streams. The microstructure of ice can be impacted directly by processes related to impurities such as Zener pinning (Smith, 1948; Humphreys and Hatherly, 2004) or grain boundary drag (Alley et al., 1986, 1989). These result in changes of the energy, shape and mobility of grain boundaries. Furthermore, impurities such as micro-inclusions directly impact deformation when they form obstacles in the ice matrix and thus enhance strain localisation and the introduction of protonic defects (Glen, 1968) or the formation of dislocation lines (Weertman and Weertman, 1992). In turn, these small-scale processes can also influence climate proxies by altering the stratigraphic integrity of impurity records (Faria et al., 2010; Ng, 2021). Therefore, understanding the localisation of impurities is important.

Over the last decades different ice cores from Greenland and Antarctica were analysed regarding the chemistry and location of impurities and the main results were recently summarised by Stoll et al. (2021b). While studies using optical microscopy by e.g., Kipfstuhl et al. (2006); Faria et al. (2010) focused mainly on the location of **insoluble water-insoluble** particles Scanning Electron Microscope (SEM) coupled with energy dispersive X-ray spectroscopy (EDS) (e.g., Wolff et al., 1988; Barnes et al., 2002; Baker et al., 2003; Barnes et al., 2003a) (e.g., Wolff et al., 1988; Baker et al., 2003; Barnes et al., 2003a) and LA-ICP-MS (e.g., Reinhardt et al., 2001; Della Lunga et al., 2014; Bohleber et al., 2020) studies also allowed the identification of impurities. They mainly found chlorine, sulphur and sodium at several locations, ranging from grain boundaries to filaments and the grain interior. However, these methods are limited to the investigation of elemental concentrations. Identifying the mineralogy of inclusions is however possible with Raman spectroscopy (e.g., Fukazawa et al., 1997; Ohno et al., 2005; Sakurai et al., 2011; Ohno et al., 2014; Eichler et al., 2019) (e.g., Fukazawa et al., 1997; Ohno et al., 2005; Sakurai et al., 2011; Eichler et al., 2019) while preserving the microstructural location, a crucial aspect regarding their impact on the physical properties of the host material. Identified inclusions in Antarctic and Greenlandic ice mainly consist of terrestrial dust (e.g., quartz, feldspar, mica, hematite) and sulphates of different chemical composition (Ca, Na, Mg, K, Al) (Ohno et al., 2005; Sakurai et al., 2009, 2011; Ohno et al., 2014; Eichler et al., 2019). Calcium carbonate ( $CaCO_3$ ) was identified by Sakurai et al. (2009) mainly in the last glacial period from the Greenland Ice Core Project (GRIP) ice core. All these **These** studies are demanding in time and costly and thus often rely on a small number of samples taken at arbitrary depths. This results in a poor understanding of **The number of identified inclusions is thus limited and the underlying processes and in a lack of identified species involved hampering the development of realistic generalisations of impurities for polar ice** (Stoll et al., 2021b).

In summary, commonly are not fully understood yet. Developing generalisations of the mineralogy and localisation of impurities in polar ice is hence still challenging (Stoll et al., 2021b).

The impurity content plays a major role regarding the physical properties of snow, firn, and ice, such as electrical conductivity (Alley and Woods, 1996; Wolff et al., 1997), permittivity (Wilhelms et al., 1998), and mechanical properties (e.g., creep behaviour, dislocation velocity) (e.g., Jones and Glen, 1969; Dahl-Jensen and Gundestrup, 1987; Paterson, 1991; Hörhold et al., 2012). Several studies investigated the impact of impurities on the deformation of ice (e.g., Jones and Glen, 1969; Petit et al., 1987; Iliescu and Baker, 2008; Eichler et al., 2019), which in turn influences the flow of ice - a major uncertainty regarding future projections of ice sheet behaviour and solid ice discharge. This chain of processes at the micro-scale resulting eventually in the large-scale deformation behaviour of ice needs to be better understood, especially in fast flowing ice, as present in ice streams. The microstructure of ice can be impacted directly by processes related to impurities such as Zener pinning (Smith, 1948; Humphreys and Hatherly, 2004) or grain boundary drag (Alley et al., 1986, 1989). These result in changes of the energy, shape and mobility of grain boundaries. Furthermore, impurities such as micro-inclusions directly impact deformation when they form obstacles in the ice matrix and thus enhance strain localisation and the introduction of protonic defects (Glen, 1968) or the formation of dislocation lines (Weertman and Weertman, 1992). In turn, these small-scale processes can also influence climate proxies by altering the stratigraphic integrity of impurity records (Faria et al., 2010; Ng, 2021).

The mineralogy of impurities, their localisation and the possible interplay between both certainly plays a role in the interaction of impurities and ice physical properties (e.g., Jones and Glen, 1969; Paterson, 1991) and ice dynamics.

Reasons for the current lack in understanding of the whereabouts of impurities in polar ice are manifold, the methodology 95 to systematically look in parallel at localisation (as a microstructural feature) and mineralogy (as a chemical feature) of micro-inclusions has just recently been developed (e.g., Eichler et al., 2019). Commonly used methods, developed to derive (paleo-) climate information on impurities such as [Continuous Flow Analysis \(CFA\)](#) **CFA** (e.g., Kaufmann et al., 2008), apply their analysis on melted sample water for the sake of decontamination and time constraints. Doing so, information on the phase and localisation of impurities are not considered. On the other hand, dedicated studies on localisation are spatially very 100 limited and do not catch the overall chemistry of a certain sample. **The mineralogy and its possible interplay for localisation was therefore not possible to investigate.** However, in order to develop a profound understanding on the mineralogy and localisation of impurities in polar ice, a combination of both approaches is needed.

With our study we attempt to push forward to combine the information of both, microstructure and chemistry, to elaborate 105 on the mineralogy of micro-inclusions in polar ice, its possible sources and its interplay with microstructure. There is no investigation of the mineralogy and location of inclusions in one polar ice core with a high enough spatial resolution and reliable statistics to generalise the spatial distribution of inclusions or to investigate the effect of different minerals on ice mechanics. We aim to gain a better understanding of the mineralogical variability of micro-inclusions inside one ice core on the large (hundreds of metres) and on the small (millimetre-centimetre) scale. Was the mineralogy of the deposited impurities stable over the last 14 ka or are there changes following the evolution of the Greenland Ice Sheet? 110 Does the mineralogy of inclusions enable a better understanding of the aerosol content of the past? Furthermore, we investigate if the location of the inclusion in the microstructure is linked to its mineralogy. Our approach is a combination of methods from microstructure and impurity research to perform a systematic high-resolution analysis along one deep ice core. The East Greenland Ice Core Project (EGRIP) ice core, the first ice core drilled through the Northeast Greenland Ice Stream (NEGIS), enables such an interdisciplinary undertaking. [A companion study investigates](#) **Stoll et al. (2021a)** investigate the location 115 of micro-inclusions and their role regarding deformation and microstructure. In this study we investigate the mineralogy of these visible micro-inclusions. We apply bulk [chemistry](#) **insoluble particle measurements** from CFA and optical microscopy and Raman spectroscopy on eleven samples along the EGRIP ice core. With this combined data set covering the Holocene [and Late Glacial](#), [the Younger Dryas](#), [and the Bølling Allerød](#), i.e. the upper 1340 m, we aim to give a systematic overview of the evolution of the mineralogy of the EGRIP ice core by identifying a relevant number of micro-inclusions at equal depth intervals. We 120 discuss the interpretation of the mineralogy of micro-inclusions in the EGRIP ice core with respect to environmental boundary conditions and survey implications for future research. **Possible formation pathways of the observed minerals are briefly discussed, but are not the main focus of this study.**

## 2 Methods

### 2.1 The East Greenland Ice Core Project

125 The EGRIP ice core drilling project is located at 75°38' N and 35°58' W, 2704 m a.s.l. (2015) on NEGIS, the largest ice stream in Greenland (Joughin et al., 2010; Vallelonga et al., 2014). At the drill site the ice flows with a velocity of  $55 \text{ m a}^{-1}$  (Hvidberg

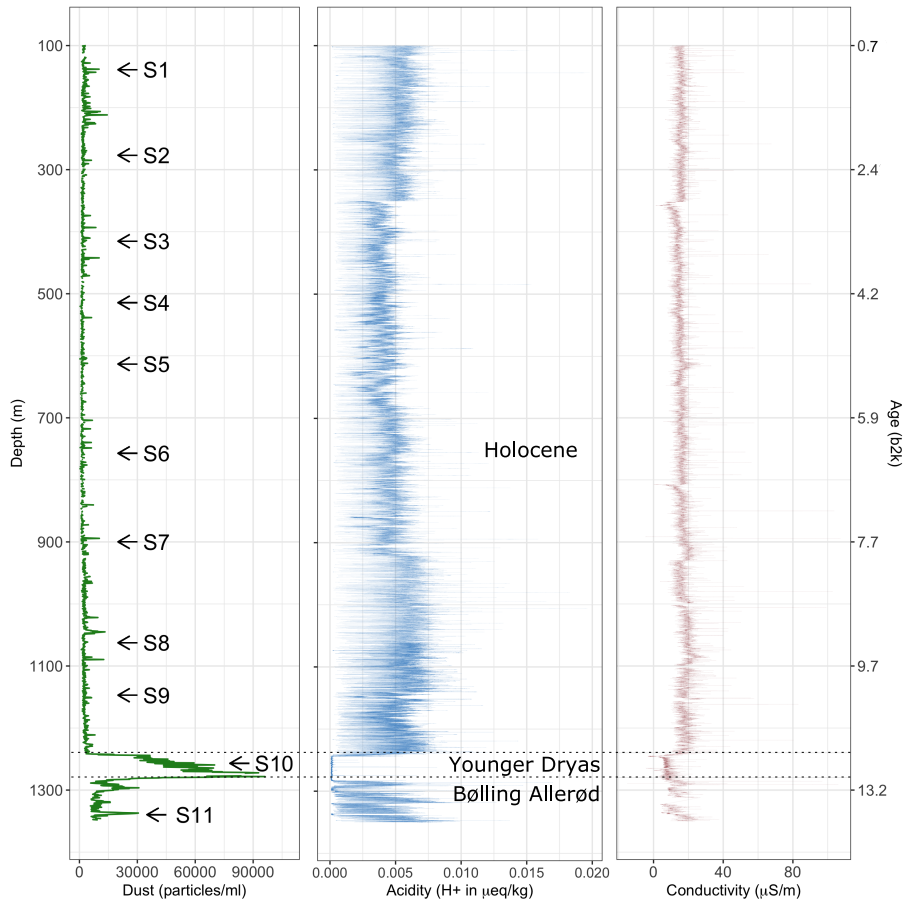


**Figure 1. Dust data** Number counts of particles larger than  $1 \mu\text{m}$  per ml of melt water (dust) derived via CFA from the upper 1340 m of the EGRIP ice core and depth regimes. Samples analysed with Raman spectroscopy. A) Mean dust particle concentrations of 55 cm bags. The green line is a locally weighted regression are indicated with a smoothing parameter of 0.3. B-L) CFA dust Acidity data from the chosen depths analysed with Raman spectroscopy Mojtabavi et al. (2020b), conductivity data from Mojtabavi et al. (2020c). The concentration range on the abscissa varies Age from Mojtabavi et al. (2020a), b2k = before 2000 CE. Sample K is within a cloudy band.

et al., 2020) offering a unique an exclusive possibility to study ice rheology and physical parameters contributing to deformation such as crystal preferred orientation and impurity content. While first results regarding the physical properties of EGRIP ice were recently published (Westhoff et al., 2020) we investigate microstructure and micro-inclusions are investigated in detail in a

130 companion paper Stoll et al. (2021a).

The present day accumulation in water equivalent at the EGRIP drill site is between 13.8 and 14.9 cm/yr (Nakazawa et al., 2021) and the averaged annual layer thicknesses for the period 1607–2011 is 0.11 m ice equivalent (Vallelonga et al., 2014). In the last 8 kyr before 2000 CE, i.e. the upper 900 m, annual layer thicknesses were almost constant, probably due to a combination of flow-induced thinning and increased upstream accumulation (Mojtabavi et al., 2020a). (Mojtabavi et al., 2020a;

135 Gerber et al., 2021). Accumulation rates were highest 7.8 kyr ago ( $0.249 \text{ ma}^{-1}$ ) and decrease towards the Last Glacial Period with a peak during the Bølling Allerød. Due to the flow of NEGIS ice from the last 8 kyr was deposited under increasingly higher accumulation rates with increasing age caused by higher precipitation closer to the ice divide (Gerber et al., 2021). Traced radar layers from the North Greenland Ice Core Project (NGRIP) drill site indicate an undisturbed climatic record of at least 51 kyr (Vallelonga et al., 2014).

140 Drilling at EGRIP has not continued since 2019 and the current drill depth is 2121 m, roughly 530 m above bedrock. We analyse the upper 1340 m of the core covering the Holocene (present-11.7 ka) in the upper 1240 m, the Younger Dryas (11.7-12.8 ka) at 1240-1280 m, and the Bølling Allerød (12.8-14.7 ka) at 1280-1375 m (Walker et al., 2018; Mojtabavi et al., 2020a). Gerber et al. (2021) propose that Last Glacial Period ice was deposited 197 to 332 km upstream from EastGRIP.

## 2.2 Continuous Flow Analysis

145 CFA data were obtained during three measurement campaigns (2018-2020) at the University of Bern using the CFA setup described in detail in Kaufmann et al. (2008) with a few minor improvements. For the analysis a longitudinal 35 x 35 mm section of the ice core was cut and melted down-core and analysed using continuous measurement methods to produce mm-cm resolution records of soluble and [insoluble water-insoluble](#) impurities in the ice. Micro-particle concentrations were determined using an Abakus (Fa Klotz) Laser Particle Sizer (e.g., Ruth et al., 2003) operating in the size range between 1-15  $\mu\text{m}$ , which 150 covers the size range of optical microscopy. The depth resolution of the data is limited by signal dispersion in the analytical system to approximately 0.5-1 cm. Depth co-registration to the [thin sections](#) [samples analysed with Raman spectroscopy](#) is limited by the accuracy of the depth assignment in the field and is typically on the order of a few mm. We calculated the arithmetic mean dust particle concentration of each [bag](#) [55 cm sample](#) for an overview.

## 2.3 Sample preparation

155 Aiming to derive a systematic overview over the EGRIP core we selected samples roughly every 100 m of depth. Samples were chosen based on a combination of depth-representative and prominent features in the CFA (e.g., high insoluble particle concentration), grain size (e.g., fine or large) and crystal preferred orientation data. The latter two are presented in [a companion paper](#) Stoll et al. (2021a), we here focus on the [chemistry](#) [mineralogy and water-insoluble particle content](#). Exact regions of 160 interests in these samples for microstructural and Raman analysis were defined using high-resolution CFA data (Fig. ??2). The chosen areas included areas without prominent properties and specific areas of interest, such as high water-insoluble particle content. We analysed eleven samples between depths of 138.92 and 1339.75 m (Fig. ?? 1 and Table 1). The nine shallower samples are from the Holocene and the two deepest from the last glacial termination (Mojtabavi et al., 2020a).

165 As described in [a companion paper](#) Stoll et al. (2021a) we used the remaining ice of the physical properties samples analysed at the EGRIP camp and created thick sections following a standard procedure (Kipfstuhl et al., 2006). No silicon oil was used to avoid artificial Raman spectra masking the micro-inclusion spectra. Most samples were approximately 10 x 10 mm, but dimensions varied (Table 1) depending on the [CFA data](#) [water-insoluble particle content](#). A Leica microtome was used to polish the top and bottom surface of the samples, which was followed by 1.5-2 hours of sublimation under controlled humidity and temperature

**Table 1.** Properties of the samples analysed with Raman spectroscopy. Acidity data from Mojtabavi et al. (2020b), conductivity data from Mojtabavi et al. (2020c).

Sample	Depth (m)	Age b2k (ka)	Size (mm x mm)	∅ Acidity (H+ in $\mu\text{eq/kg}$ )	∅ Conductivity ( $\mu\text{S/m}$ )
138.92 S1	138.9-138.913	1.0	13.01 x 16.96	$5.7 \cdot 10^{-3}$	19.2
276.88 S2	276.87-276.881	2.2	11.00 x 12.76	$4.7 \cdot 10^{-3}$	14.3
415.30 S3	415.305-415.315	3.5	10.01 x 13.27	$1.4 \cdot 10^{-3}$	16.4
514.44 S4	514.435-514.445	4.3	9.94 x 60.60	$3.0 \cdot 10^{-3}$	13.5
613.30 S5	613.30-613.32	5.2	17.31 x 54.19	$3.2 \cdot 10^{-3}$	12.4
757.21 S6	757.17-757.25	6.4	90.00 x 16.78	$3.7 \cdot 10^{-3}$	17.2
899.98 S7	899.965-899.975	7.6	11.32 x 12.62	$6.1 \cdot 10^{-3}$	18.4
1062.65 S8	1062.645-1062.655	9.3	9.67 x 8.47	$4.0 \cdot 10^{-3}$	14.0
1141.17 S9	1141.158-1141.175	10.2	16.61 x 21.67	$3.5 \cdot 10^{-3}$	15.8
1256.96 S10	1256.945-1256.956	12.1	10.45 x 48.50	$4.1 \cdot 10^{-4}$	7.18
1339.75 S11	1339.735-1339.747	14.1	11.24 x 11.96	$3.6 \cdot 10^{-3}$	13.9

b2k=before 2000 CE (Mojtabavi et al., 2020a)

conditions. Thus, a good sample surface quality was obtained and small-scale disturbances (e.g., microtome scratches) were erased while grain-boundary grooves became more distinct. Polished surfaces allow the localisation of micro-inclusions 500

170  $\mu\text{m}$  below the sample surface and successful Raman spectroscopy measurements with strong signals.

## 2.4 Microstructure mapping and impurity maps

Microstructure mapping was performed following Kipfstuhl et al. (2006) and Eichler et al. (2017) and the detailed investigation of the microstructural location of micro-inclusions is explained in detail in a companion paper Stoll et al. (2021a). Samples were placed under an optical Leica DMLM microscope with an attached CCD camera (Hamamatsu C5405) and several hundred 175 individual photomicrographs were created grid-wise with a scanning resolution of  $3 \mu\text{mpix}^{-1}$ . The creation of high-resolution maps to detect micro-inclusions provided the basis for a structured Raman analysis. These inclusions are usually 1-2  $\mu\text{m}$  in diameter (Fig. 4A) and consist of droplets, dust particles or salts. We focused inside the ice using transmission light mode and different focus depths to locate micro-inclusions below the surface (Fig. 3B). Microstructure maps with indicated micro-inclusions are from now on called "impurity maps". We mapped grain boundaries on the sample surface and translated them into 180 the impurity map (Fig. 3) by applying a grain boundary width of 300  $\mu\text{m}$ . This is an upper-limit assumption and compensates for vertically tilted grain boundaries and internal light diffraction with depth (Eichler et al., 2017). Micro-inclusions inside these grain boundaries were classified as "at the grain boundary" (Fig. 3C).

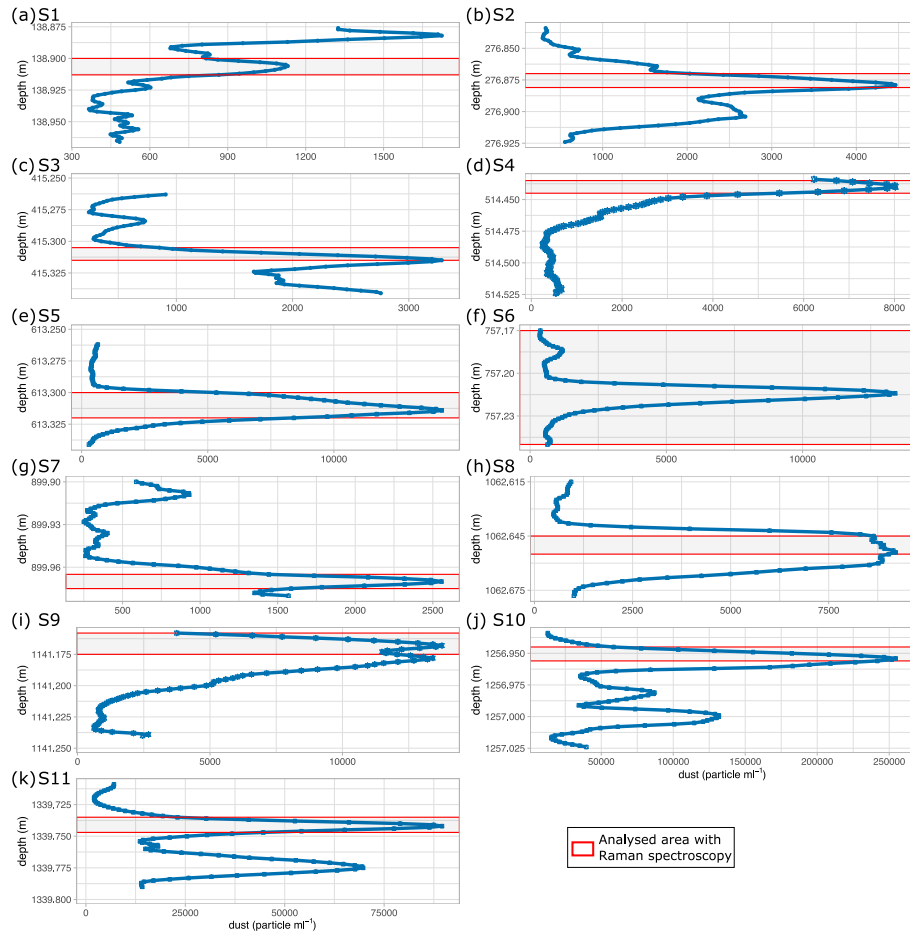


**Figure 2.** Details Number counts of the analysis procedure on the sample from a depth of 1339.75 m. Grain boundaries are indicated with 300 insoluble particles larger than 1  $\mu\text{m}$  thick violet lines. Localised micro-inclusions 500  $\mu\text{m}$  below per ml (dust) derived via CFA from the surface are indicated by yellow circles; micro-inclusions chosen depths analysed with Raman spectroscopy are indicated by filled blue circles with white crosses. Out of focus black shapes are air bubbles. A) Map of Please note the sample surface with highlighted grain boundaries, different scales in dust concentration on the arrow indicates the surface of the ice sheet abscissa. B) Impurity map with S10 is within a focus depth of 500  $\mu\text{m}$  below the sample surface cloudy band, micro-inclusions and grain boundaries are indicated. C) Detail a horizontal layer of much higher dust content than the area indicated in B. D) Identified Raman spectra of the micro-inclusions indicated in C. One inclusion consists of a quartz above and gypsum spectra simultaneously below.

## 2.5 Cryo-Raman spectroscopy

The Raman effect is the inelastic scattering of light caused by the excitation of vibrational modes of crystals or molecules. This results in the Raman shift – a loss of scattered light energy, which is specific for each vibrational mode (Raman and Krishnan, 1928). The Raman shift is used to identify chemical impurities in samples in a non-destructive way – Raman spectroscopy. It is well suited for light-transparent materials, such as ice (e.g., Fukazawa et al., 1998; Weikusat et al., 2012; Eichler et al.,

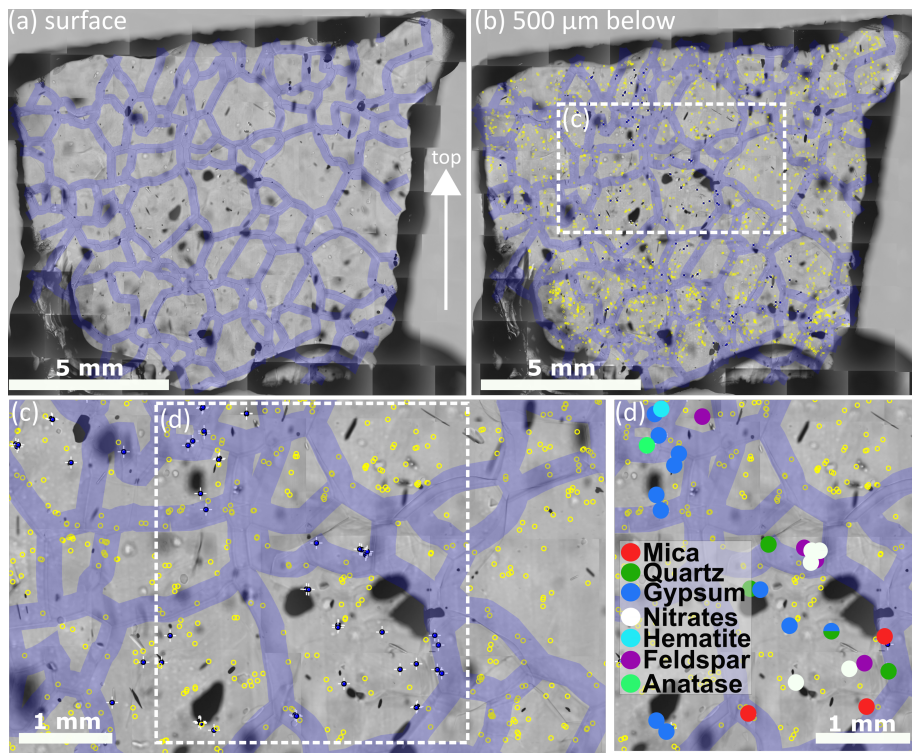


**Figure 3.** Details of the analysis procedure on S11 (1339.75 m). Grain boundaries are indicated with 300  $\mu\text{m}$  thick violet lines. Localised micro-inclusions 500  $\mu\text{m}$  below the surface are indicated by yellow circles; micro-inclusions analysed with Raman spectroscopy are indicated by filled blue circles with white crosses. Out of focus black shapes are air bubbles. A) Map of the sample surface with highlighted grain boundaries, the arrow indicates the surface of the ice sheet. B) Impurity map with a focus depth of 500  $\mu\text{m}$  below the sample surface, micro-inclusions and grain boundaries are indicated. C) Detail of the area indicated in B. D) Identified Raman spectra of the micro-inclusions indicated in C. One inclusion consists of a quartz and gypsum spectra simultaneously.

2019). Using confocal optics, it is possible to focus the excitation laser on a small volume segment (few  $\mu\text{m}^3$ ) inside the sample (Fig. 4A). The same confocal optics collect the backscattered light, which is conducted into a spectrometer to resolve 190 the spectral distribution. Due to the low probability of a photon being Raman-scattered long integration-times, high incident light intensities and sufficient particle concentration is needed. To avoid melting, laser power is limited and thus, well-prepared sample surfaces and precise focusing of the laser is essential to obtain identifiable spectra (Fig. 4B-D) (Eichler et al., 2019).

Spectroscopy analysis was performed at the Alfred Wegener Institute Helmholtz Centre for Polar- and Marine Research, Bremerhaven with a WITec alpha 300 M+ combined with a NdYAG laser ( $\lambda = 532\text{ nm}$ ) and a UHts 300 spectrometer with a 600 grooves  $\text{mm}^{-1}$  grating. The used Raman system is further described by Weikusat et al. (2015). The 195 microscope unit is located in a small cold lab inside an insulated cabin with a temperature of -15°C. The control unit, spectrometer and excitation laser are located close to the cell at room temperature and connected with the microscope. We used a 100  $\mu\text{m}$  fibre to obtain a good compromise between signal intensity and confocality. If necessary, samples

were re-polished in the same cabin, allowing fast and controlled sample sublimation and a low risk of contamination. The  
200 small cabin volume resulted in increasing temperatures over time; measurements were stopped at the very latest at -8°C. To avoid extensive sublimation measurements were continued on the next day. Sample analysis was carried out until a maximum of ~500  $\mu\text{m}$  from the sample surface sublimated. However, we were able to analyse high numbers of micro-inclusions, often exceeding 100 micro-inclusion measurements per sample. Raman spectra were background corrected and identified using reference spectra (e.g., Ohno et al., 2005; Eichler et al., 2019), and the RRUFF project database  
205 (Lafuente et al., 2015) (examples in 4B-D).

When using Raman spectroscopy on micro-inclusions inside ice, the ice spectrum is always present (Fig. 4B-D). Other factors hampering clear Raman signals are: 1) small sizes of micro-inclusions, 2) laser beam path length, 3) quality of sample surface, and 4) acquisition time. Normally, one micro-inclusion was measured ten times with an acquisition time of 0.5-2 s per spectrum, resulting in a total acquisition time of at least 5 s. Weak signals were remeasured with up to 3 s per spectrum and  
210 thus, up to 30 s in total. The potential cumulative heating of the micro-inclusion limits the total acquisition time, because it could result in melting of the sample or the destruction of the inclusion.

We measured in a maximal focus depth of 500  $\mu\text{m}$  below the surface to obtain high-quality signals (Fig. 3B). Surface pollution and possible reactions or rearrangements of elements on the surface were avoided by focusing into the sample, thus only analysing inclusions in the ice. Nevertheless, this leads to a permanent superimposition of the ice spectrum. Impurity  
215 peaks were well distinguishable in most cases, even though some signals with strong ice-vibrational bands were hidden by the Raman-active ice spectra. This is often the case for O-H signals of hydrates, which are luckily shifted to higher frequencies in minerals and normally very strong – distinguishing them was usually possible.

Spectroscopy analysis was performed at the Alfred Wegener Institute Helmholtz Centre for Polar- and Marine Research, Bremerhaven with a WITec alpha 300 M+ combined with a NdYAG laser ( $\lambda = 532\text{ nm}$ ) and a UHts 300 spectrometer with a 600 grooves  $\text{mm}^{-1}$  grating. The used Raman system is further described by Weikusat et al. (2015). The  
220 microscope unit is located in a small cold lab inside an insulated cabin with a temperature of -15°C. The control unit, spectrometer and excitation laser are located close to the cell at room temperature and connected with the microscope. We used a 100  $\mu\text{m}$  fibre to obtain a good compromise between signal intensity and confocality. If necessary, samples were re-polished in the same cabin, allowing fast and controlled sample sublimation and a low risk of contamination. The small cabin volume resulted in increasing temperatures over time; measurements were stopped at the very latest at -8°C. To avoid extensive sublimation measurements were continued on the next day. Sample analysis was carried out until a maximum of ~500  $\mu\text{m}$  from the sample surface sublimated. However, we were able to analyse high numbers of micro-inclusions, often exceeding 100 micro-inclusion measurements  
225 per sample. Raman spectra were background corrected and identified using reference spectra (e.g., Ohno et al., 2005; Eichler et al., 2019), and the RRUFF project database (Lafuente et al., 2015) (examples in 4B-D).

### 3 Results

#### 3.1 Evolution of **insoluble** water-insoluble particle number with depth

To put the samples analysed for micro-inclusions into a broader context, Fig. ??1 shows a profile of 55 cm average micro-particle concentrations over the entire depth range of the core. Generally, during the Holocene, particle concentrations are relatively low, compared to the Preboral and Younger Dryas periods in good agreement with previous studies of micro-particle  
230

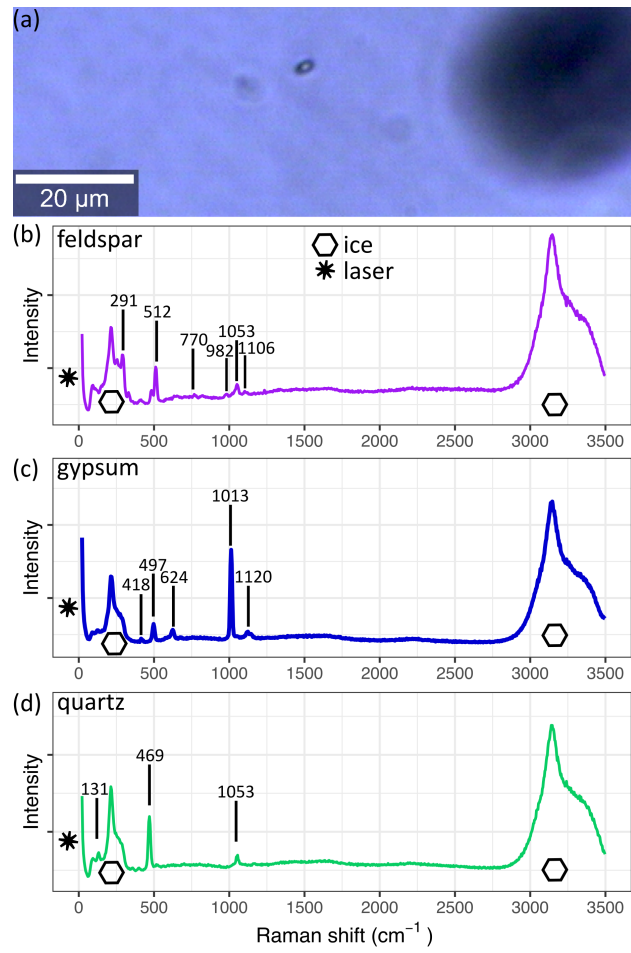


**Figure 4.** A micro-inclusion at in S11 (1339.75 m of depth) as seen with the 20x lens of the Raman system. The derived spectrum of the inclusion is shown in B). The spectra in C) and D) are from the same sample and frequently measured throughout the core. Superimposed ice and laser signals are indicated. A) The small black object is a micro-inclusion, the larger black object out of focus is an air bubble. B) Observed spectra of feldspar. C) Observed spectra of gypsum. D) Observed spectra of quartz.

concentrations in Greenland ice (Steffensen, 1997; Ruth et al., 2003). However, a detailed climatological interpretation of the data, including e.g., possible upstream effects, is outside the scope of this study and will follow at a later time.

Mean particle numbers are generally consistent and vary most for example at a depth of 210 m. The general increase in insoluble water-insoluble particle numbers with depth also occurs in our chosen samples and is up to two orders of magnitude from the shallowest to the deepest samples (Fig. ??B-L2).

The four shallowest samples show insoluble water-insoluble particle peaks between 1400 and 8000  $ml^{-1}$  (Fig. ??B-E2A-D), while the highest values are observed in the three deepest samples (up to  $>250000 ml^{-1}$ ) (Fig. ??J-L2I-K). There is a high variability of the insoluble water-insoluble particle concentration on small spatial scales and significant changes occur within

240 centimetres due to the pronounced seasonality in the dust deposition in Greenland. Fig. ??K) and ??L) display insoluble 2J) and 2K) display water-insoluble particle numbers skyrocketing and dropping over a few centimetres.

**Table 2.** Most abundant Raman spectra in EGRIP Holocene ice and localisation data. Mg- and K-sulphate minerals could not be identified clearly. Sulphates, except gypsum, at grain boundaries were not distinguished and are indicated with hyphens. Details on grain boundary statistics are shown in Table 1 in Stoll et al. (2021a).

Mineral	Number	Absolute at GB	Relative at GB (%)	Spatial pattern	Formula
Sulphates	386	92	23.8	clusters and layers	$XSO_4$
Gypsum	170	47	27.6	throughout	$CaSO_4 * 2H_2O$
Quartz	126	28	22.2	NA	$SiO_2$
Mica	81	22	27.2	limited area	$(K, Na, Ca, NH_4)Al_2(Si_3Al)O_{10}(OH)_2$
Feldspar	67	21	31.3	NA	$(K, Na, Ca, NH_4)(Al/Si)_4O_8$
Mg-sulphate	64	-	-	clusters and layers	$MgSO_4$
Bloedite	61	-	-	clusters and layers	$Na_2Mg(SO_4)_2 * 4H_2O$
Nitrates	39	9	25	throughout	$XNO_3$
Hematite	33	8	24.2	NA	$Fe_2O_3$
K-sulphate	31	-	-	clusters and layers	$K_2SO_4$
Krohnkite	27	-	-	clusters and layers	$Na_2Cu(SO_4)_2 * 2H_2O$

GB=grain boundaries, NA=no common pattern

### 3.2 Raman spectra and derived mineralogy

We conducted Raman spectroscopy on several of the previously located micro-inclusions from all eleven samples. Analysed inclusions were chosen randomly, but with the intention to represent the entire area of the sample. The use of confocal mode 245 and a 20x and 50x lens allowed us to find more than 97 % of the micro-inclusions indicated in our impurity maps. The number of analysed micro-inclusions per sample ranged from 47 to 134 and a total of 791 spectra were identified. Luminescence was present in 131 measurements, which were excluded. Micro-inclusions with no obtained Raman signal could be Raman-inactive or the Raman signal might be superimposed by the ice signal, i.e. too low in intensity to be identified with confidence. Some analysed micro-inclusions showed Raman spectra of more than one mineral. We classified these complex micro-inclusions 250 (Fig. 3D and Fig. 8B) as one spectra of each type regardless of the relative strength of the Raman peak as done by e.g., Sakurai et al. (2011).

We identified 26 different Raman signals, which can be mainly differentiated into mineral dust and sulphates. An overview is presented in Fig. 5 and the most abundant minerals are displayed in Table 2 (all spectra are displayed in Table A1). Mineral dust minerals are primarily silicates such as quartz and members of the feldspar or mica group. Less abundant dust minerals are hematite, rutile and anatase (both  $TiO_2$ , rutile is the high-temperature form), titanite ( $CaTiSiO_5$ ), jacobsite ( $MnFe_2O_4$ ). 255 Sulphates Sulphate minerals (from now on "sulphates") can be difficult to distinguish due to tiny differences in their Raman

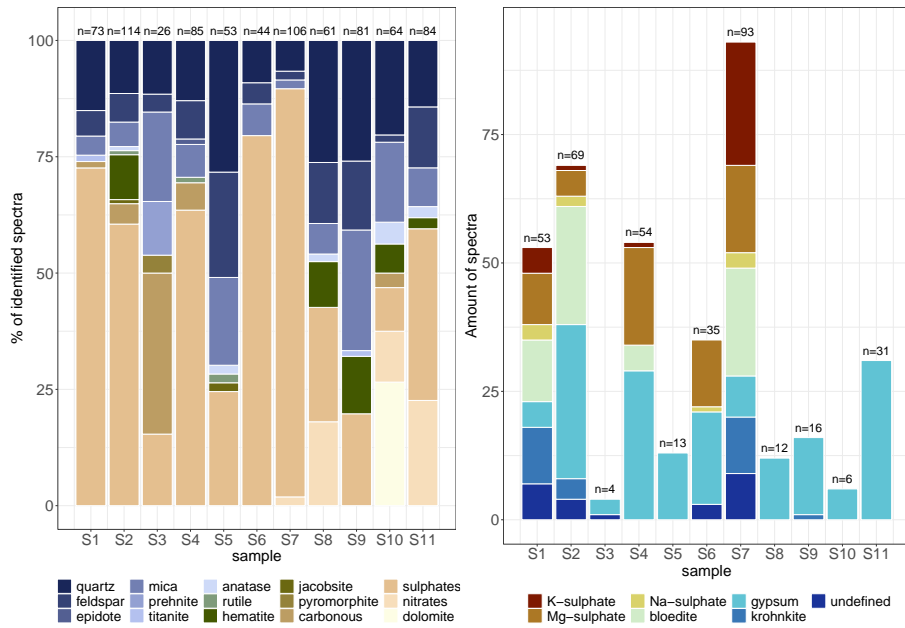


**Figure 5.** Identified Raman spectra of micro-inclusions in EGRIP Holocene ice, n is the total amount of identified spectra per sample. The two deepest samples are from the [Younger Dryas](#) and Bølling Allerød and have by far the highest [insoluble water-insoluble](#) particle concentrations. A) All identified Raman spectra per sample. For better visibility some Raman spectra are condensed in groups (e.g., sulphates and mica). B) Identified sulphates in detail. Sulphate diversity decreases below 900 m.

spectra, but most sulphates were identified (Fig. 5B). Most abundant are gypsum, Mg-sulphate, and bloedite. Less abundant are krohnkite, Na-, and K-sulphates. Spectra with a strong peak at  $1050\text{ cm}^{-1}$  [probably](#) indicate K-nitrates while a strong peak around  $1070\text{ cm}^{-1}$  [might indicate indicates](#) Na-nitrates (Ohno et al., 2005). The carbonate mineral dolomite ( $\text{CaMg}(\text{CO}_3)_2$ ) was identified [at in S10 \(1256.96 m\)](#) in large quantities. We further measured Raman spectra [which might be of](#) carbonaceous particles (C), [pyromorphite \( \$\text{Pb}\_5\(\text{PO}\_4\)\_3\text{Cl}\$ \)](#), [prehnite \( \$\text{Ca}\_2\text{Al}\_2\text{Si}\_3\text{O}\_{10}\(\text{OH}\)\_2\text{Ca}\_2\text{Al}\_2\text{Si}\_3\text{O}\_{10}\(\text{OH}\)\_2\$ \)](#), [pyromorphite \( \$\text{Pb}\_5\(\text{PO}\_4\)\_3\text{Cl}\$ \)](#), and [epidote \( \$\text{Ca}\_2\(\text{Fe}/\text{Al}\)\text{Al}\_2\(\text{Si}\_2\text{O}\_7\)\(\text{SiO}\_4\)\text{O}\(\text{OH}\)\$ \)](#), the latter [three](#) [two](#) were only found once. It is likely that the carbonaceous particles originate from biomass combustion, i.e. black carbon.

### 3.3 Mineral diversity with depth

Between eight and 17 different spectra were identified per sample, the median value is 10 different spectra per sample (Fig. 6A). To compare our samples despite the varying amount of total identified Raman spectra per sample we calculated a diversity index  $I_{var}$  with the ratio of the amount of different minerals per sample ( $n_m$ ) to the total amount of identified micro-inclusions per sample ( $n_i$ ) and the amount resulting in the diversity index  $I_{var}$  with a maximum of 1.  $I_{var}$  of different minerals per sample ( $n_m$ ):

$$I_{var} = \frac{n_i}{n_m}$$

270 1 indicates that every inclusion is of different mineralogy while values close to 0 indicate a homogeneous mineralogy.

Mineralogy diversity increases

$$I_{var} = \frac{n_m}{n_i} \quad (1)$$

$I_{var}$  varies between 0.099 and 0.308, the mean value is 0.158 (Fig. 6B). Mineralogy diversity decreases slightly with depth. Deeper samples are slightly more diverse in mineralogy even though, the large diversity of sulphates is only found in the upper 900 m (Fig. 275 5B). As expected, samples with larger numbers of identified Raman spectra tend to be more diverse in mineralogy supporting the use of  $I_{var}$ .

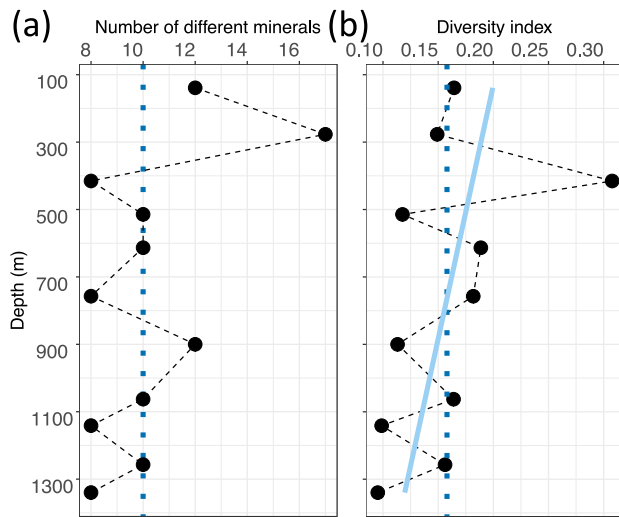


**Figure 6.** Mineral number and diversity with depth in EGRIP ice. A) Absolute numbers of different minerals per sample. The dotted blue line is the median value (10). B) Diversity index values calculated after Eq. (1). The light blue line is a linear regression, the dotted blue line is the mean value (0.158). Higher values indicate a larger mineral diversity in relationship to the amount of identified Raman spectra per sample.

### 3.4 Spatial patterns revealed by mineralogy

#### 3.4.1 Large-scale: Mineralogy evolution along the ice core

The relative abundance of the three silicates quartz, feldspar and mica often correlates, with increased values at the same depths (e.g., at 276.88 m, 613.3 m, 1062.65 m S2, S5, S8). Quartz represents between 6.6 % (899.94 m S7) and 28.3 % (613.3 m S5), feldspar between 280 1.6 % (1256.98 m S10) and 22.6 % (613.3 m S5), and mica between 1.9 % (899.94 m S7) and 25.9 % (1141.2 m S9) of all identified micro-inclusions at one depth. These minerals dominate the sample from 613.3 m of depth S5 and the three samples between 900 and 1257 m (S8, S9, S10). The deepest sample S11 shows an additional high amount of sulphates, i.e. gypsum (Fig. 5). Minerals, such as hematite, titanite or nitrates or titanite, were only found in the samples below 900 m. Nitrates were found at 899.98 m in S7 and were among the main impurities in three of the four deepest samples, i.e. at 1062.65, 1256.96 and 1339.75 m of depth S8, S10, and S11.

285 Dolomite was only identified at 1256.96 m of depth in S10. Carbonaceous particles were found in the four shallowest samples (138.92, 276.88, 415.3, 514.44 m) and at a depth of 1256.96 m in S1, S2, S3, and S4) and in S10.

The majority of sulphates was found in the seven shallowest samples below a depth of 900 m (Fig. 5B). Over the core sulphate spectra represent between 9.4 % (1256.98 m S10) and 87.7 % (899.94 m S7) of all identified micro-inclusions at one depth. As displayed in Fig. 5B and briefly described in Sect. 3.3 various different sulphates are found above 900 m while the only sulphates below 900 m are gypsum and , at 1256.96 m, one krohnkite micro-inclusion in S10. Gypsum sometimes follows the abundance pattern of the terrestrial dust minerals (at 276.88 m, 514.44 m, 1141.17 m in S2, S4, and S9).

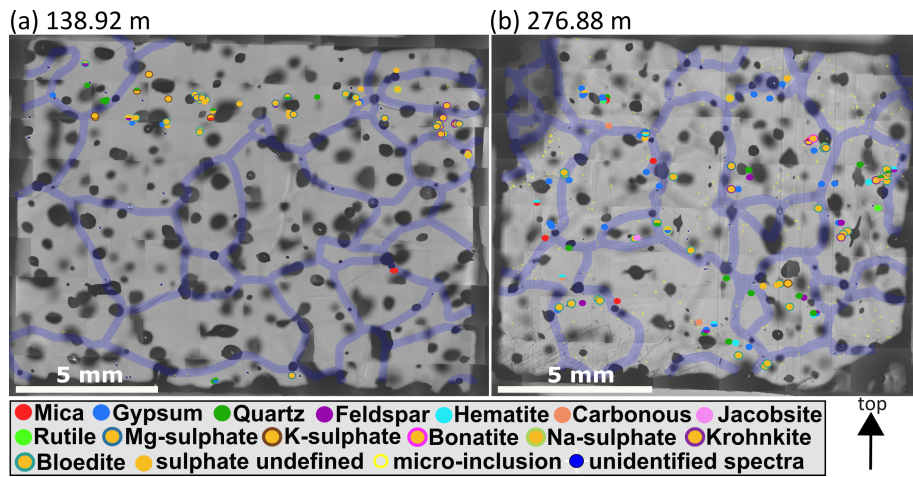


**Figure 7.** Impurity maps from a depth of S1 (138.92 m) and S2 (276.88 m). Identified micro-inclusions are represented by filled circles with different colours; sulphates are orange circles with differently coloured contours. Transparent violet lines are 300  $\mu\text{m}$  thick grain boundaries, the arrow points towards the surface of the ice sheet. A) A layer of sulphate micro-inclusions is in the upper part of the sample, below are almost no micro-inclusions. B) A wide variety of different Raman spectra and spatial patterns, e.g. clusters and rows of sulphates.

### 3.4.2 Small-scale: Clusters

Dense clusters of micro-inclusions (minimum of three proximal inclusions) of the same mineralogy were observed throughout the core, but especially above 900 m (e.g., at 138.92, 514.44, 757.21, and 899.98 m S1, S4, S6, and S7). Specifically sulphates at these 295 depths were often found in such clusters (Fig. 7 and 8A, B). The abundance of such clusters of micro-inclusions with similar chemistry declines with depth and is rarely observed below 900 m. Certain minerals, such as mica, only occur in a limited area of the sample (e.g., at 1339.75 m in S11) without creating distinct layers or clusters. Gypsum and nitrates were found throughout the entire sample area while no specific localisation was identified for minerals such as quartz, hematite or nitrates (Table 2).

### 3.4.3 Small-scale: Horizontal layers

300 Often micro-inclusions of the same mineralogy are found in distinct layers horizontal to the core axis (distinct vertical layers were not observed) or broader bands. Fig. 8A shows that at a depth of 757.2 m ([S6](#)) mineralogy changes on the centimetre-scale. The shallowest part of the sample is characterised by a mixture of sulphates (mainly gypsum) and terrestrial dust (quartz, feldspar, mica). Some centimetres deeper a small layer of gypsum is followed by a layer of mainly Mg-sulphates. At the bottom of the sample Mg-sulphates dominate, accompanied by gypsum and mica.

305 A broad layer is observed at 899.98 m ([S7](#)) (Fig. 8B). The upper three quarters of the sample are dominated by different sulphates, especially the middle section shows a clear layer. Sulphates in this layer are often found in clusters. The deepest part of the sample inhibits a broader variety of minerals, ranging from different sulphates to mica and quartz (Fig. 8B).

### 3.4.4 Small-scale: Localisation at grain boundaries

181 identified micro-inclusions were located at grain boundaries, i.e. in the upper-limit assumption of 300  $\mu\text{m}$  thick grain 310 boundaries. 92 sulphate particles (including 47 gypsum inclusions) were found at grain boundaries, followed by quartz (28), mica (22), feldspar (21), nitrates (9), hematite (8), and anatase and titanite (both 1). In relation to the total number of each mineral 31.3 % of feldspar, 27.6 % of gypsum, 27.2 % of mica, 23.8 % of sulphate (including gypsum, 20.8 % without gypsum), and 22.2 % of quartz was located at grain boundaries.

The relative amount of sulphates at grain boundaries was higher [at depths in samples](#) with a high diversity in sulphate types, 315 i.e. [at 138.92, 276.88, 514.44, 613.3, 757.21, and 899.98 m](#) [S1, S2, S4, S5, S6, and S7](#), than the relative amount of terrestrial dust located at grain boundaries. Below 900 m feldspar, mica and quartz were more common at grain boundaries than sulphates, i.e. gypsum. However, [at 1339.75 m in S11](#) 37.9 % of all identified micro-inclusions at grain boundaries were gypsum.

## 4 Discussion

In this study we have shown that the [insoluble water-insoluble](#) particle content is variable on the centimetre-scale, but increases 320 with depth. Furthermore, the mineralogy of micro-inclusions in EGRIP ice varies on the large-scale, i.e. throughout the core, and on small spatial scales, i.e. centimetres. [The accompanying data from the applied](#) [Applying different](#) methods (CFA, microstructure-mapping, and Raman spectroscopy) enabled us to create high-resolution impurity maps showing that sulphates and terrestrial dust are the most abundant minerals. The upper 900 m are characterised by sulphates with a diverse mineralogy while mineral dust [minerals](#) and gypsum dominate below. Spatial patterns of inclusions of the same mineralogy were revealed, ranging from 325 distinct layers of several millimetre thickness to clusters (mainly of sulphates).

### 4.1 [Insoluble Water-insoluble](#) particles at EGRIP

We here present the 55 cm [bag](#) [mean CFA results of the insoluble](#) [sample mean water-insoluble](#) particle number (Fig. ??1), representing the dust concentration in the ice. [Though, detailed studies will follow in the future, we can already see, that the insoluble micro-particle concentration](#) , interpreted as

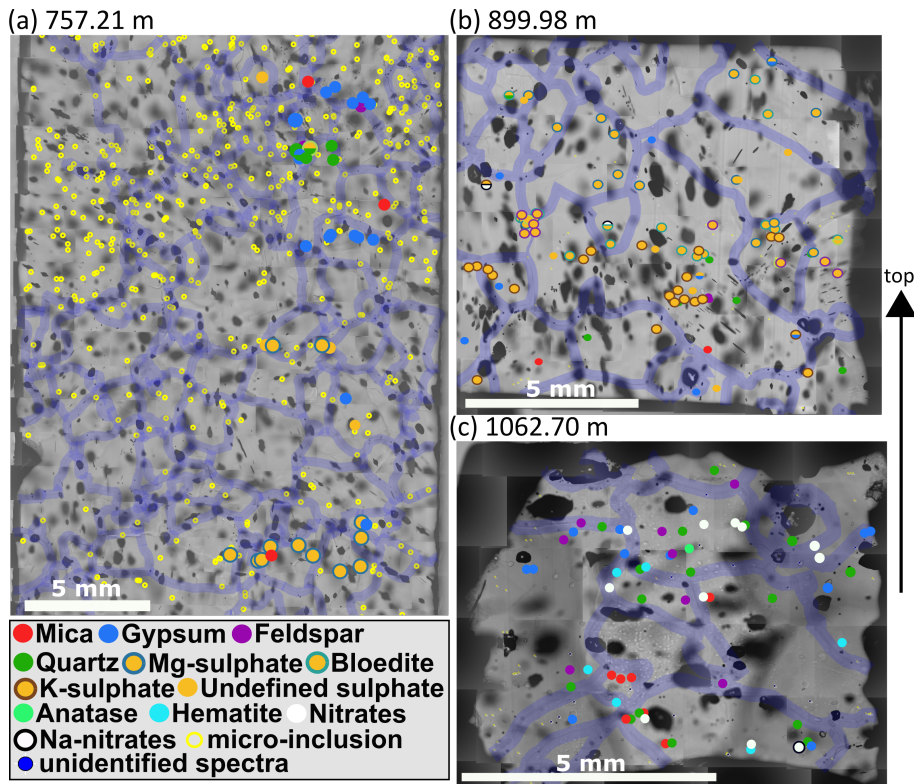


**Figure 8.** Impurity maps from a depth of 757.21 (S6), 899.98 (S7), and 1062.7 (S8) m. Same annotations as in Fig. 7. A) Mineralogy changes within centimetres along the vertical axis. The shallower part is dominated by gypsum and terrestrial dust while the deeper part is dominated by Mg-sulphates. B) A strong sulphate layer is found in the middle of the sample, terrestrial dust is mainly found below. C) Mineralogy differs strongly from the shallower samples: sulphates are less diverse, mineral dust and nitrates dominate, and clusters are less common.

the mineral dust aerosol particle record, seems to vary We find the particle concentration to vary with depth, indicating changes in mineral dust through the Holocene. The concentration is comparable to e.g., the North Greenland Ice Core Project ice core (Steffensen et al., 2008) and is low in overall concentration compared to Glacial ice (e.g., Steffensen, 1997; Ruth et al., 2003).

High concentrations of insoluble particles measured with CFA water-insoluble particles correlate with areas of numerous micro-inclusions observed with optical microscopy and Raman spectroscopy. The samples with the highest insoluble water-insoluble particle counts, i.e. at depths of 1256.96 and 1339.75 m S10 and S11, are from the Younger Dryas and the Bølling Allerød. This explains the much higher insoluble water-insoluble particle concentration, compared to our Holocene samples (Fig. ??1), which is closer to resemble concentrations found in Glacial ice (Ruth et al., 2003). The highest amount of insoluble water-insoluble particles measured with CFA is at 1256.96 m of depth in S10 (Fig. ??2J), inside a cloudy band. Cloudy bands originate from seasonal events, such as atmospheric storms, resulting in increased transport and deposition of impurities on the ice sheet (Svensson et al., 2005). This explains the high number of mineral dust minerals, the low number of sulphates measured with Raman spectroscopy (Fig. 5A) and the resulting higher  $I_{var}$  compared to the deepest sample S11. It further supports the hypothesis that insoluble

water-insoluble dust contributes significantly to cloudy bands (Svensson et al., 2005). The unique location of the EGRIP drill site on an ice stream and the assumed high impact of high-impurity layers on the deformation of the ice (e.g., Dahl-Jensen and Gundestrup, 1987; Paterson, 1991; Miyamoto et al., 1999) highlight the need for an in-depth study of cloudy bands at EGRIP.

We adjusted the approach of using CFA data for efficient Raman analysis (Eichler et al., 2019) and conclude that analysing 345 insoluble water-insoluble particle data first on the large-scale, i.e. along one ice core (Fig. ??A1), followed by small-scale analysis, i.e. over centimetres (Fig. ??B-L2A-K), provides an excellent basis for a systematic analysis of different depth regimes while ensuring a sufficient number of micro-inclusions. Combined with microstructure-mapping it additionally accelerates the time-consuming search for micro-inclusions, especially in pure Holocene ice.

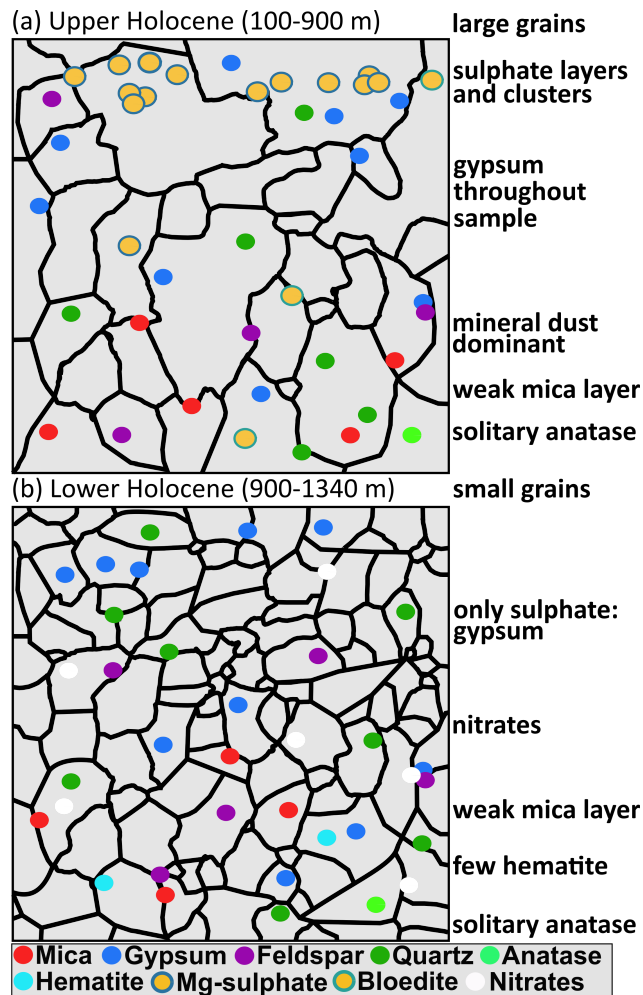


**Figure 9.** Sketch of the simplified distributional patterns of minerals found in A) upper Holocene ice and B) lower Holocene ice.

## 4.2 Abundance of minerals Minerals in EGRIP ice

### 350 4.2.1 Abundance of minerals

In general, our results show a large abundance of minerals across all samples while depth-related differences occur in total, and relative, mineral abundance. A detailed discussion of the observed shift change in mineralogy over the EGRIP ice core is presented in Sect. 4.2.2.

355 The most abundant minerals are sulphates and terrestrial dust minerals, which agrees with observations by e.g., Ohno et al. (2005); Sakurai et al. (2009); Eichler et al. (2019). Antarctic ice analysed by Ohno et al. (2005, 2006); Sakurai et al. (2010, 2011) and Eichler et al. (2019) is dominated by sulphates, they represent e.g., up to 96 % of all identified spectra in the interglacial samples of Eichler et al. (2019). Contrary to this, our samples show, in general, a higher diversity in minerals as displayed in Fig. 6. Only the sample from 899.98 m of depth has a comparable amount of sulphates (87.7 % of all identified spectra). We identified most sulphates as gypsum or Na-sulphates, which agrees with e.g., Ohno et al. (2005); Eichler et al. (2019) (Fig. 5B).

360 We observed a total of 170 gypsum micro-inclusions making it the most abundant mineral and the only sulphate which occurs in every sample supporting e.g., Legrand and Mayewski (1997) and Sakurai et al. (2009). Legrand and Mayewski (1997) show that  $CaSO_4$  and  $MgSO_4$  can be produced if terrestrial compounds, such as  $MgCO_3$  and  $CaCO_3$ , are neutralised with  $H_2SO_4$ . They also found  $CaSO_4$  in Holocene ice from Greenland despite a low  $Ca^{2+}$  concentration.

365 Contrary to gypsum, krohnkite is a globally rare sulphate mineral. This is reflected in its small absolute number (27, see Table 2) compared to most of the other identified sulphates. Mineral dust, such as feldspar, mica and quartz, were abundant at all depths, but generally in lower abundances than gypsum (Table 2). These minerals were especially abundant at a depth of 613.3 m (S5) and in the deepest sample close to the Glacial (S11). The Glacial sample analysed by Eichler et al. (2019) shows a similar abundance of terrestrial dust minerals.

370 We observed nitrates at depths between 899.94 and 1339.75 m in S7, S8, S10 and S11. Nitrates were also found with Raman spectroscopy by Fukazawa et al. (1998); Ohno et al. (2005), while Sakurai et al. (2009) and Eichler et al. (2019) observed nitrate-ions only with IC, not with Raman spectroscopy. Nitrates are a major impurity component in polar ice as obtained from CFA (Röthlisberger et al., 2000b) and IC (Eichler et al., 2019) analyses, but there is a lack of understanding in which form they are present in ice. For example, sulfuric acid competes with other acids to react with the relative rare cations, replaces other acids in their salts and thus forms a variety of sulphate salts (Iizuka et al., 2008). The relative abundance of nitrates at a certain depth (Fig. 5A) indicates that similar processes occur with nitrates. However, nitrate ions seem to be more likely to exist in dissolved forms than in particle forms as suggested by Eichler et al. (2019). The secondary minerals pyromorphite and epidote were each only found once. Prehnite was identified three times. 375 Jacobsite was found twice (S2 and S5).

Antarctic ice is dominated by sulphates (Ohno et al., 2005, 2006; Sakurai et al., 2010, 2011; Eichler et al., 2019), they represent e.g., up to 96 % of all identified spectra in the interglacial samples of Eichler et al. (2019). Contrary to this, our samples show, in general, a higher diversity in minerals as displayed in Fig. 6. Only the sample from 899.98 m of depth (S7) has a comparable amount of sulphates (87.7 % of all identified spectra).

## 380 4.2.2 Shift Change in mineralogy

We have observed a pronounced shift change in mineralogy from a sulphate and terrestrial dust-dominated sulphate-diverse, while terrestrial dust rich, regime in the upper 900 m to a terrestrial dust-dominated regime with partially high amounts of gypsum . (Fig. 5). The lack of a variety of sulphate minerals below 900 m is shown in our diversity index, which decreases with depth even though other minerals occur at these depths, such as dolomite. Similar findings were reported by earlier studies (e.g., 385 Ohno et al., 2005; Sakurai et al., 2009; Eichler et al., 2019) who found sulphates and mineral dust in varying numbers, but our systematic approach exposes the mineral diversity already present in Holocene ice in more detail.

Sulphates The most common minerals, i.e. sulphates and terrestrial dustminerals , are found throughout the entire ice core, but in varying abundance (Fig. 5 and simplified in Fig. 9). Rare minerals, such as hematite, anatase and titanite were found at all independent of depths. Other minerals e.g., rutile and epidote, were only found in shallow samples while e.g., dolomite and 390 nitrates were only found in deep samples. The high abundance of sulphates in many samples can be explained by the formation of sulphates after initial deposition (Ohno et al., 2005).  $Na^+$  and  $Mg^{2+}$ , the main cations combining with  $SO_4^{2-}$ , could originate from blown-in sea salt ( $NaCl$  and  $MgCl_2$ ), which was deposited on the ice sheet and, during transport, has partially chemically reacted with acidic compounds as proposed by Artaxo et al. (1992); Kerminen et al. (2000) for Antarctic sea salt. However, deeper samples show smaller amounts, and varieties, of sulphates, which almost completely disappear below 900 m. In the four deepest samples gypsum is the only sulphate, except for one Krohnkite micro-inclusion at 1141.17 m. in S9. Data is scarce Data 395 were scarce until now, but e.g., Sakurai et al. (2009, 2011) and Eichler et al. (2019) show that sulphates are found in deeper parts of ice sheets, also consisting almost entirely of gypsum supporting our results.

Even though we found a shift in mineralogy, this shift find this difference in mineralogy between the upper and lower part, this change does not correlate with a major change of the climate period, i.e. from Glacial to Holocene ice. Eichler et al. (2019) found a strong difference in mineralogy between Interglacial and Glacial ice in the EDML ice core. However, main minerals 400 in Interglacial ice are sulphates (especially Na-sulphate and gypsum) while mineral dust and gypsum dominate in Glacial ice (Eichler et al., 2019). Ohno et al. (2005) show that salt inclusions consist mainly of Na- and Mg-sulphates in Holocene ice from Dome Fuji, Antarctica while gypsum and nitrate salts dominate in the Last Glacial Maximum. This agrees with our findings and could indicate that, in Greenland and Antarctica, compounds bearing a variety of sulphates are more abundant in warm 405 periods, such as the Holocene or the Eemian, while mineral dust and gypsum dominate during cold periods, such as the last Glacial. However, it is interesting that the transition from the Holocene to the Stadial is not represented by a major change in mineralogy. An investigation of 410 EGRIP glacial samples will show if prominent changes in mineralogy also occur in deeper depth than the analysed upper 1340 m.

#### 4.2.3 Detailed comparison with mineralogy in the GRIP ice core

A limited number of polar ice cores have been drilled over the last decades and mineralogy data is are only available for a few 410 of those. The relatively close to EGRIP located drill site of In Greenland, the GRIP ice core was analysed with Raman spectroscopy and EDS by Sakurai et al. (2009). We The GRIP and EGRIP drill sites are relatively close by, we thus compare both cores here in detail.

We found gypsum at all depths at EGRIP resembling the results by Sakurai et al. (2009). Similar to our findings, Na- and Mg-sulphates, quartz, and nitrates are less abundant in their samples. Sakurai et al. (2009) analysed 6.9 and 9.8 ka BP old samples, which we compare to our 6.4 ka (S6), 9.3 ka (S8), and 10.2 ka (S9) old samples. The younger samples from both 415 studies are mainly composed of gypsum, Na- and Mg-sulphates, and smaller amounts of quartz, feldspar, and mica. In the 9.8 ka old sample Sakurai et al. (2009) found gypsum, slightly less Na- or Mg-sulphate and some "other" minerals while our 9.3 ka and 10.2 ka old samples (S8 and S9) show a slightly different mineralogy. Quartz is dominant in both samples and is accompanied by gypsum, feldspar and, to varying degrees, mica. Both samples contain no sulphates except gypsum and krohnkite. Gypsum is the only sulphate in our oldest sample S11 (14.1 ka), which agrees well with the 13.5 ka sample from 420 Sakurai et al. (2009).

The higher **relative** amount of terrestrial minerals in our samples is difficult to explain conclusively, because the GRIP and EGRIP sites are comparably close to each other and in similar distances to the coast. **At certain depths Intentionally choosing samples with a high water-insoluble particle content could partly explain this observed difference. In certain samples, e.g., at 613.3, 1062.65, and 1256.96 m S5, S8, and S10,** the majority of micro-inclusions consists of mineral dust, which might indicate 425 strong dust storms or deposition events as proposed for cloudy bands by e.g., Svensson et al. (2005). However, we show that the diversity in mineralogy can be high within centimetres (e.g., Fig. 8). The observed differences are thus probably caused by natural variability amplified by methodological differences, such as different sample sizes.

#### 4.2.4 Methodological drawbacks

We can not determine if rarely found minerals only occur at certain depths, or if this is related to statistics drawbacks. Minerals, 430 such as hematite and anastase, were only found in a few samples while rutile, titanite, epidote, and jacobsite have only been found **once in one sample**. Unfortunately, the problem of statistics reoccurs in microstructural impurity research, which can only be partly solved by analysing larger samples, and with a higher spatial resolution **which is not always feasible due to the amount of work needed for the analysis**.

Furthermore, there are known drawbacks of Raman spectroscopy, such as the inability to identify Raman-inactive compounds, the superimposition of the ice spectra, and the focus on visible, undissolved impurities. Especially the main component 435 of sea salt, NaCl, is inaccessible with Raman spectroscopy and thus not considered in our analysis.

Some Raman spectra **from a depth of 415.3 in S3** were difficult to identify. **We, we** thus had to exclude several spectra, **further lowering the already small number of observations**. However, analysing inclusions inside the ice prevents contamination and preserves their in situ locations and is thus a well justified approach.

440 **Obtaining good Raman spectra and identifying them with enough confidence will always be a challenge.** We could not identify all measured Raman spectra similar to other studies using this method. As an example we measured the same unknown spectra as presented in Fig. 2G by Sakurai et al. (2011). **Obtaining good Raman spectra and identifying them with enough confidence will always be a challenge.** These technical limitations hamper a fully holistic analysis and are difficult to overcome. A partial solution would be an analysis of the same samples with a subsidiary method **which identifies location and chemistry of impurities**,

445 such as SEM coupled with EDS or LA-ICP-MS. Such a combined analysis would enable a deeper insight into the EGRIP ice core and into impurities in polar ice in general.

#### 4.3 Possible reasons for the diversity of minerals in EGRIP ice

We observed a prominent diversity in mineralogy of micro-inclusions in EGRIP ice across all scales. Mineral abundance changes throughout the core, i. e. the observed shift in sulphate diversity (Sect. 4.2.2), and across samples, i. e. in distinct layers and clusters (Sect. 3.4). This can partly be explained methodologically, Raman spectroscopy 450 data do not allow insights into the specific formation pathways of the identified inclusions. However, we give a brief overview of the most likely origins or formation pathways of the major groups of minerals, and of some rare minerals.

##### 4.3.1 Mineral dust

Dust minerals, such as quartz, feldspar, hematite, mica, and carbonates, usually originate from desert regions where 455 strong winds erode crustal material. The small, sub-micron, particles can then be transported over long distances by the prevailing winds. As the particles are crustal material the most abundant elements are consequently Si, Al, Fe and their mineralogy can depend on the source regions. These particles represent the chemical composition of the crust and the most abundant elements are consequently Si, Al, and Fe.

##### 4.3.2 Sulphates

The high abundance of sulphates in many samples can be largely explained by blown-in sulphate-bearing compounds 460 from the continents (e.g., gypsum) or from sea salt (e.g., by the number of analysed micro-inclusions per sample, by different deposition conditions, or by chemical reactions taking place in the ice.  $Na_2SO_4$ ) (Legrand and Mayewski, 1997). However, it is suggested that sulphate minerals can also form after initial deposition when acidic aerosols of sulphuric acid, such as  $H_2SO_4$  droplets, gain cations from other sources (e.g., Ohno et al., 2005). The main cations of the sulphate minerals in our samples are  $Ca^{2+}$ ,  $Mg^{2+}$ , and  $Na^+$  (Table 2). Ohno et al. (2005) suggest that  $Mg^{2+}$  and  $Na^+$  could originate from blown-in sea salt ( $NaCl$  and 465  $MgCl_2$ ), which was deposited on the ice sheet. This would result in the possibility that HCl and  $Cl^-$  enter the ice lattice creating point defects and thus effecting the electric conductivity (Petrenko and Whitworth, 1999; Ohno et al., 2005) and dislocation mobility (e.g., Hu et al., 1995). HCl solution is monoatomic and without a vibrational spectrum and thus not detectable with Raman spectroscopy. We are limited in evaluating the process of sulphatisation in our samples, but our results imply that the process proposed by Ohno et al. (2005) could occur.

470 A difference in the chemistry at the ice sheet surface at the time of deposition and different atmospheric circulation patterns, and thus varying aerosol input, could be indicated by our CFA data. The difference in sulphate diversity between shallower and deeper samples could be explained by a difference in available dust (Fig. ??1 and 2). Iizuka et al. (2012) concluded that aerosol sulfatation sulphatisation in Antarctica is proportional to the dust flux and more likely to occur in the atmosphere or during fallout than after deposition. For Greenland, the major dust source areas for the Last Glacial and the Younger Dryas were the East Asian deserts (Svensson et al., 2000; Valletlonga and Svensson, 2014) with minor contributions from the Sahara (Han 475 et al., 2018). Aerosols deposited in the Holocene are likely from the Takla Makan and Gobi desert (Bory et al., 2003; Valletlonga and Svensson, 2014). These differences in dust input

between the Holocene and the Last Glacial are represented in our results. During the Holocene, sea salt aerosols reacted with acid-gas particles during transport and in the snowpack. In the Glacial however, acids were often neutralised by the higher amounts of terrestrial dust, i.e. with high concentrations of  $Ca^{2+}$ , and thus reacted less with sea salt (Röthlisberger, 2003). Fittingly, our results show that high dust concentrations often correlate with the dominance of gypsum over other sulphate minerals 480 while lower dust values correlate with medium to high numbers of Na- and Mg-sulphates.

#### 4.3.3 Nitrates

Nitrates are well soluble in water and nitrate salts are often found as nitratine ( $NaNO_3$ ) in arid regions, our inclusions are thus presumably of detrital origin. However, nitrates are a major impurity component in polar ice as obtained from CFA 485 (Röthlisberger et al., 2000b) and IC (Eichler et al., 2019) analyses, but there is a lack of understanding in which form they are present in ice. For example, sulphuric acid competes with other acids to react with the relative rare cations, replaces other acids in their salts and thus forms a variety of sulphate salts (Iizuka et al., 2008). The relative abundance of nitrates at a certain depth (Fig. 5A) indicates that similar processes occur with nitrates. However, nitrate ions seem to be more likely to exist in dissolved forms than in particle forms due to their good solubility in water.

#### 4.3.4 Rare minerals

490 The rarely observed minerals pyromorphite, epidote, prehnite, and jacobsite are most likely of detrital origin and were transported together with more common dust minerals. The micrometre-sizes of the inclusions indicate a distant source region, such as the deserts of Asia (Bory et al., 2003; Vallelonga and Svensson, 2014).

Pyromorphite and epidote are secondary minerals and were only found once. Pyromorphite is usually found in the 495 oxidised zones of lead ore deposits. Epidote is abundant in e.g., the highest  $I_{var}$  value was measured in the deepest sample originating from the Bølling Allerød. The strong layering and clustering of sulphates could originate from dry deposition events, which form deposition crusts mainly containing sulphates. Another possible aspect is the unique impact of NEGIS. Older samples originate from further upstream than younger samples, which could be reflected in the micro-inclusion mineralogy. However, we do not expect any major upstream deposition effects during the Holocene, but this should be verified in future studies. A systematic follow-up study on EGRIP Glacial 500 ice is needed to investigate if the observed trends, e.g., of mineral diversity and clustering, continue with depth schistose rocks or marble. It can be a product of the hydrothermal alteration of minerals in igneous rocks, such as feldspar or mica. Prehnite was identified three times and is normally found in Mg- or Fe-rich (i.e. mafic) volcanic rocks and can be a product of hydrothermal alteration in chasms or veins. Jacobsite was found twice (S2 and S5) and can occur as a primary phase or as a product of the metamorphism of manganese deposits and thus, altered manganese minerals. It is typically associated with, among others, hematite and both were identified in S2. Fe-minerals, such as hematite and jacobsite, were identified in this study and occur relatively often in polar ice (e.g., Baccolo et al., 2018; Eichler et al., 2019; Baccolo et al., 2021). Baccolo et al. (2018) showed that 505 the deep ice sheet environment is not anoxic and dissolved oxygen and liquid water veins might support the oxidation and dissolution of specific mineral phases. Investigating such specific chemical reactions of Fe-minerals is beyond the scope of this study, but they display the lack of knowledge regarding ice as a chemical reactor.

#### 4.3.5 Chemical reactions in ice

Another possibility explaining the diversity in chemical compounds are chemical reactions occurring inside the ice as summarised for snow by Bartels-Rausch et al. (2014), and discussed for ice by Steffensen (1997); de Angelis et al. (2013); Baccolo et al. (2018) and Eichler et al. (2019). Time spans of several thousand years could enable that impurities in the ice react and thus, led to post-depositional changes in the composition of impurities. Barnes et al. (2003b); Masson-Delmotte et al. (2010); de Angelis et al. (2013) suggest movement of chloride and sulphate ions after deposition while Barnes and Wolff (2004) report of possible reactions between dust particles and soluble impurities. Baccolo et al. (2018) suggest that, for iron, oxidation and dissolution are the main processes taking place in deep samples from the Talos Dome, Antarctica ice core. The deep ice sheet environment is not anoxic and dissolved oxygen and liquid water veins might support the oxidation and dissolution of specific mineral phases (Baccolo et al., 2018). Fe-minerals occur relatively often in polar ice and were identified in this study and by e.g., Baccolo et al. (2018); Eichler et al. (2019); Fe was found by e.g., Obbard and Baker (2007); Della Lunga et al. (2014). Furthermore, Faria et al. (2010) observed the formation of solid inclusions in deep ice, which was supported by Eichler et al. (2019). A local mixing of impurities in shear bands with high strain rate and strain could explain the observed our observations of clustering of sulphates (Eichler et al., 2019). There might be local and is not unlikely due to the dynamic conditions inside NEGIS. Local small-scale processes involved leading could lead to preferred clustering of micro-inclusions with similar chemistry. We observed preferred clustering at all depths, however samples below 900 m show significantly fewer clusters. This correlates with the depth of declining sulphate-diversity and could indicate that, around this depth, certain unknown chemical reactions occur or that large-scale boundary conditions, such as climate or ice sheet extent, changed during the time of deposition. Furthermore, visual stratigraphy data (Weikusat et al., 2020) and the core break record show that the brittle zone, the transition from air bubbles to clathrates hydrates (Ohno et al., 2004; Neff, 2014), at EGRIP is roughly at 550-1000 m of depth. Defects in the ice matrix, grain boundaries and micro-inclusions can act as nucleation sites for hydrate nucleations (Ohno et al., 2010). We found most clathrates below 900 m evoking the possibility that this transition zone also impacts sulphate chemistry, but details are unknown.

#### 4.4 Mineralogy related to Holocene climate as derived from ice cores and its possible imprint in mineralogy

We observed a prominent diversity in mineralogy of micro-inclusions in EGRIP ice across all scales. Mineral abundance changes throughout the core, i.e. the observed change in sulphate diversity (Sect. 4.2.2), and across samples, i.e. in distinct layers and clusters (Sect. 3.4). This can be partly explained by different deposition conditions throughout the Holocene which we briefly discuss here.

Previous studies have suggested two possible scenarios for the Holocene climate evolution. It was either a a stable period of climate with the Holocene Thermal Maximum in the Mid-Holocene (9-5 ka BP), or a period with a rather long-term cooling trend and an earlier, stronger Holocene Thermal Maximum (Axford et al., 2021). The prominent change of abundant minerals at a depth of 900 m could be explained by these two scenarios leaving different imprints on the mineralogy.

The extension of the Greenland Ice Sheet during the Holocene cannot be constrained exactly, and it probably differed significantly between regions (Lecavalier et al., 2014; Young and Briner, 2015). The rapid retreat of the ice sheet in NE-Greenland 12 ka ago lead to ice-free coastal areas in NE-Greenland after ~9 ka BP (Lecavalier et al., 2014)(Lecavalier et al., 2014;

Simonsen et al., 2019). Air temperatures over Greenland increased in the Holocene Thermal Maximum and peaked  $\sim$ 7.8 ka BP (Lecavalier et al., 2014; Axford et al., 2021) exposing bedrock and thus enabling . The average EGRIP annual layer thickness is surprisingly constant during the Holocene, but a significant change occurs around 7-8 ka b2k (Mojtabavi et al., 2020a). The RECAP dust record shows the exposition of local dust sources. , e.g., in King Christian X land, between  $12.1 \pm 0.1$  and  $9.0 \pm 0.1$  ka b2k (Simonsen et al., 2019). Syring et al. (2020) show that the sea ice cover in NE-Greenland transformed from a reduced state towards a marginal, almost extended, state between Early ( $\sim$ 11.7-9 ka BP) and Mid Holocene ( $\sim$ 9-5 ka BP) possibly impacting the input of sea salt, a major source of sulphates. The variability in sulphate diversity and number could display the variety in blown-in sea salt aerosols carrying sulphate compounds, such as gypsum. Even though the main dust input to Greenland was from East Asia (Svensson et al., 2000; Bory et al., 2003), regional changes (e.g., exposed bedrock) might have had an impact on the availability of chemical compounds in the air, and thus during deposition. However, this is unlikely due to the high elevation of EGRIP (2700 m) and the upstream effect caused by NEGIS, but detailed isotopic and mineralogical analyses are needed to test this. The occurrence of other sulphates than gypsum in 9.8 ka old GRIP ice (Sakurai et al., 2009) supports a site specific, regional difference at EGRIP compared to GRIP. A major change in aerosol chemistry and ion composition deposited at EGRIP is however unlikely, but upcoming studies are needed to discuss the chemical evolution at the site. The average EGRIP annual layer thickness is surprisingly constant during the Holocene and a significant change occurs around 7-8 ka b2k (Mojtabavi et al., 2020a), but the involved upstream effect of NEGIS and the general history of the ice stream are not well understood, thus hampering the further investigation of these, spatial and temporal, large-scale processes. Visual Stratigraphy and the core break record show that the brittle zone, the transition from air bubbles to clathrates hydrates (Ohno et al., 2004; Neff, 2014), at EGRIP is roughly at 550-1000 m of depth. Defects in the ice matrix, grain boundaries and micro-inclusions can act as nucleation sites for hydrate nucleations (Ohno et al., 2010). We found most clathrates below 900 m evoking the possibility that this transition zone also impacts sulphate chemistry, but details are unknown.

560 This brief evaluation of possibilities shows that chemical reactions and differences in A difference in the chemistry at the salt-formation conditions in the ice are the most likely explanation, as ice sheet surface at the time of deposition and different atmospheric circulation patterns, and thus varying aerosol input, could be indicated by the micro-particle record (Fig. 1). Dust particle numbers generally increase with depth (Fig. 2) and especially S10 is from a dust-rich period, the Younger Dryas. For Greenland, the major dust source areas for the Last Glacial and the Younger Dryas were 565 the East Asian deserts (Svensson et al., 2000; Vallelonga and Svensson, 2014) with minor contributions from the Sahara (Han et al., 2018). Aerosols deposited in the Holocene are likely from the Takla Makan and Gobi desert (Bory et al., 2003; Vallelonga and Svensson, 2014). These differences in dust input between the Holocene and the Last Glacial are represented in our results, e.g., suggested for differences in micro-inclusion chemistry between Dome Fuji Holocene and Interstadial ice (Ohno et al., 2005). It is thus necessary to investigate the redistribution of impurities, and their chemical reactions (including their rates), in ice sheets. Samples with a high number of identified Raman spectra 570 mostly showed a higher diversity in mineralogy, which leads to the lowest  $I_{var}$  value was measured in the deepest sample originating from the Bølling Allerød. The strong layering and clustering of sulphates observed in some samples could originate from dry deposition events, which form deposition crusts mainly containing sulphates.

575 Another possible aspect is the conclusion that more extensive impurity studies are needed to get comprehensive results. At this point, we can only suggest explanations for the change in diversity of sulphates, but upcoming studies on impact of NEGIS. Our analysed samples were deposited within 197 km upstream from EGRIP and thus at slightly higher surface elevations ( $2993 \pm 7$  m a.s.l. at 1400 m depth), which limits

the impact on the aerosol input. Accumulation rates for ice from depths of 900 to 1400 m were low, except the peak during the Bølling Allerød (Gerber et al., 2021). This peak coincides with a low  $I_{var}$  value in S11 displaying that a high accumulation rate does not necessarily lead to mineral diversity. However, it is difficult to compare the Holocene samples to the two samples from the Younger Dryas and Bølling Allerød. A systematic follow-up study on EGRIP Glacial ice is 580 needed to investigate if the observed trends, e.g., the bulk chemistry of EGRIP Holocene ice and flow effects of NEGIS might deliver crucial information to fully explain it of mineral diversity, continue with depth.

## 4.5 Outlook

The data presented in this study and its companion paper show the need to aim for a more holistic and in-depth understanding of the, macro- and micro-scale, processes in polar ice. Progressing towards an improved synoptic view is only possible by broader collaborations between the involved diverse research fields (microstructure, paleo-processes, impurities) 585 applying different methods. Therefore, it is needed to clearly define method-related limitations, to develop concepts to tackle these limitations while systematically combining their strengths. Especially the broad field of cryo-related impurity research has a variety of methods to measure dissolved and undissolved impurities, but they are mainly applied solitarily and results are often only partly transferable. To illustrate this point we briefly summarise the (simplified) capabilities of established methods regarding their ability to measure 590 dissolved or undissolved impurities. IC measures dissolved (and a fraction of undissolved) impurities while Raman spectroscopy measures a limited number of undissolved particles, such as the micro-inclusions analysed in this study. CFA melts the ice, where an unknown fraction of insoluble particles in the ice go into solution. The remaining insoluble particles are measured by the particle sensor of the CFA, giving a relative number of particle concentration of the original ice. Finally, ICP-MS and LA-ICP-MS measure all, dissolved and 595 undissolved, particles but information on the fraction of both impurity states are lost. To illustrate this point we briefly summarise the (simplified) capabilities of established methods regarding their ability to measure dissolved or undissolved impurities. IC measures dissolved (and a fraction of undissolved) impurities while Raman spectroscopy measures a limited number of undissolved particles, such as the micro-inclusions analysed in this study. CFA melts the ice, where an unknown fraction of water-insoluble particles in the ice go into solution. The remaining water-insoluble particles are measured by the particle sensor of the CFA, giving a relative number of particle concentration of the original ice. Finally, ICP-MS and LA-ICP-MS measure all, dissolved and undissolved, particles but information on the fraction of both impurity states are lost. Recent work by Ng (2021) demonstrates the 595 challenge up ahead of better understanding climate signal records in deep polar ice and how these signals could be affected by processes involving grain boundaries, microstructure, veins, and impurities.

Our presented data and drawn conclusions demonstrate that our systematic approach is a good way towards a more detailed understanding of impurities, i.e. their mineralogy and 600 location, in polar ice. It emphasises the importance of systematically analysing different spatial scales with a variety of methods to achieve holistic results. Despite the comparably high absolute number of identified micro-inclusions statistics are still improvable, especially for minerals which occur rarely such as hematite or anatase. Further in-depth analysis of EGRIP Glacial ice could help to improve statistical certainty. A comprehensive understanding of the mineralogy and location of impurities in our samples could be reached by analysing our samples with a complimentary method, such as LA-ICP-MS or SEM and EDS.

## 5 Conclusions

We here derive the first systematic analysis of the mineralogy of micro-inclusions in Holocene and Late Glacial ice from the 605 EGRIP ice core, the first deep ice core from a fast flowing ice stream. More specific, we derived dust particle concentration along the upper 1340 m via CFA and analysed micro-inclusions in detail with a combination of optical microscopy and Cryo-Raman spectroscopy at eleven different depths. Combining these methods, and thus covering different scales, provides a 610 good basis for a systematic analysis of different depth regimes while ensuring a sufficient number of micro-inclusions.

By identifying almost 800 Raman spectra we obtained new qualitative, and quantitative, insights into the mineralogy of 615 micro-inclusions in polar ice. 26 different spectra were identified, which indicates a more diverse mineralogy in ice from the last 14 ka than previously observed. In general most inclusions are sulphates, especially gypsum, and mineral dust, such as quartz, mica, and feldspar. Sulphates in the upper 900 m tend to create clusters of similar chemical composition and mineral

diversity ~~increases~~ ~~decreases~~ slightly with depth. The ~~here analysed~~ 1340 m of the EGRIP ice core [analysed here](#) can be divided into two depth regimes of different mineralogy. The upper 900 m are characterised by various sulphates while below this depth 615 gypsum is the only sulphate. This might be explained by different ~~, yet uncharted, chemical reactions occurring in the ice or by amounts of water-insoluble particle input, other reasons might be~~ large-scale changes in NE-Greenland during the Mid-Holocene, such as the decreasing lateral extent of the Greenland Ice Sheet revealing bedrock at the coast or the varying sea-ice cover impacting the availability of sulphates in the air during deposition. [Further studies are however needed to define exact reasons.](#)

Our study emphasises the need to overcome technical limitations, which could be achieved by an inter-method comparison 620 of e.g., Raman spectroscopy, LA-ICP-MS and SEM. However, our systematic overview of the mineralogy of micro-inclusions throughout a large part of one deep ice core helps to develop a better understanding of the role of impurities in polar ice.

## Appendix A: Appendix A

**Table A1.** Identified Raman spectra in the upper 1340 m of the EGRIP ice core.

Mineral	Number	Formula
Gypsum	170	$CaSO_4 * 2H_2O$
Quartz	126	$SiO_2$
Mica undefined	42	$(K, Na, Ca, NH_4)Al_2(Si_3Al)O_{10}(OH)_2$
Feldspar	67	$(K, Na, Ca, NH_4)(Al/Si)_4O_8$
Mg-sulphate	64	$MgSO_4$
Bloedite	61	$Na_2Mg(SO_4)_2 * 4H_2O$
Nitrates	36	$XNO_3$
Hematite	33	$Fe_2O_3$
K-sulphate	31	$K_2SO_4$
Krohnkite	27	$Na_2Cu(SO_4)_2 * 2H_2O$
Mica (Phlogopite)	25	$KMg_3(Si_3Al)O_{10}(OH, F)_2$
Sulphate undefined	24	$XSO_4$
Carbonous	22	C
Dolomite	17	$CaMg(CO_3)_2$
Mica (Muscovite)	25	$KAl_2(Si_3Al)O_{10}(OH, F)_2$
Na-sulphate	9	$NaSO_4$
Anatase	8	$TiO_2$
Rutile	3	$TiO_2$
Mica (Paragonite)	3	$NaAl_2(Si_3Al)O_{10}(OH)_2$
Prehnite	3	$Ca_2Al_2Si_3O_{10}(OH)_2$
Na-nitrates	3	$NaNO_3$
Jacobsite	2	$MnFe_2O_4$
Titanite	2	$CaTiSiO_5$
Epidote	1	$Ca_2(Fe/Al)Al_2(Si_2O_7)(SiO_4)O(OH)$
Pyromorphite	1	$Pb_5(PO_4)_3Cl$
Air	1	$O_2$

*Data availability.* Raman data and high-resolution microstructure and impurity maps are available at PANGAEA. CFA data will be published separately with an in-depth CFA study.

625 *Author contributions.* Conceptualisation by NS, IW, and MH. Microstructure mapping and Raman methodology developed by NS, JE, and IW, CFA methodology by TE and CJ. Investigation and Data curation by NS, TE, and CJ. Formal analysis by NS and TE. Funding acquisition for NS by IW. The original draft was written by NS with assistance from all co-authors.

*Competing interests.* The authors declare that the research was conducted in the absence of any commercial or financial relationships that could be construed as a potential conflict of interest.

630 *Acknowledgements.* This work was carried out as part of the Helmholtz Junior Research group “The effect of deformation mechanisms for ice sheet dynamics” (VH-NG-802). We thank all EGRIP participants for logistical support, ice processing and fruitful discussions. EGRIP is directed and organised by the Centre for Ice and Climate at the Niels Bohr Institute, University of Copenhagen. It is supported by funding agencies and institutions in Denmark (A. P. Møller Foundation, University of Copenhagen), USA (US National Science Foundation, Office of Polar Programs), Germany (Alfred Wegener Institute, Helmholtz Centre for Polar and Marine Research), Japan (National Institute of 635 Polar Research and Arctic Challenge for Sustainability), Norway (University of Bergen and Trond Mohn Foundation), Switzerland (Swiss National Science Foundation), France (French Polar Institute Paul-Emile Victor, Institute for Geosciences and Environmental research), Canada (University of Manitoba) and China (Chinese Academy of Sciences and Beijing Normal University). TE and CMJ gratefully acknowledge the long-term financial support of ice core research at the University of Bern by the Swiss National Science Foundation (grant no. 200020\_172506 (iCEP) and 20FI21\_164190 (EGRIP).

640 **References**

Alley, R., Perepezko, J., and Bentley, C. R.: Grain Growth in Polar Ice: I. Theory, *Journal of Glaciology*, 32, 415–424, <https://doi.org/10.3189/S0022143000012132>, 1986.

Alley, R. B. and Woods, G. A.: Impurity influence on normal grain growth in the GISP2 ice core, Greenland, *Journal of Glaciology*, 42, 255–260, 1996.

645 Alley, R. B., Blankenship, D. D., Rooney, S. T., and Bentley, C. R.: Water-pressure coupling of sliding and bed deformation: III. Application to Ice Stream B, Antarctica, *Journal of Glaciology*, 35, 1989.

Artaxo, P., Rabello, M. L. C., Maenhaut, W., and Grieken, R. V.: Trace elements and individual particle analysis of atmospheric aerosols from the Antarctic peninsula, *Tellus B*, 44, 318–334, <https://doi.org/10.1034/j.1600-0889.1992.00010.x>, 1992.

Ashby, M. F.: Boundary defects and the mechanism of particle movement through crystals, *Scripta Metallurgica*, 3, 843–848, 650 [https://doi.org/https://doi.org/10.1016/0036-9748\(69\)90192-6](https://doi.org/https://doi.org/10.1016/0036-9748(69)90192-6), 1969.

Axford, Y., de Vernal, A., and Osterberg, E. C.: Past Warmth and Its Impacts During the Holocene Thermal Maximum in Greenland, *Annual Review of Earth and Planetary Sciences*, 49, 081 420–063 858, <https://doi.org/10.1146/annurev-earth-081420-063858>, 2021.

Baccolo, G., Cibin, G., Delmonte, B., Hampai, D., Marcelli, A., Stefano, E. D., Macis, S., and Maggi, V.: The Contribution of Synchrotron Light for the Characterization of Atmospheric Mineral Dust in Deep Ice Cores : Preliminary Results from the Talos Dome Ice Core ( East 655 Antarctica ), *Condensed Matter*, 3, <https://doi.org/10.3390/condmat3030025>, 2018.

Baccolo, G., Delmonte, B., Niles, P. B., Cibin, G., Di Stefano, E., Hampai, D., Keller, L., Maggi, V., Marcelli, A., Michalski, J., Snead, C., and Frezzotti, M.: Jarosite formation in deep Antarctic ice provides a window into acidic, water-limited weathering on Mars, *Nature Communications*, 12, 1–8, <https://doi.org/10.1038/s41467-020-20705-z>, <http://dx.doi.org/10.1038/s41467-020-20705-z>, 2021.

Baker, I., Cullen, D., and Iliescu, D.: The microstructural location of impurities in ice, *Canadian Journal of Physics*, 81, 1–9, 660 <https://doi.org/10.1139/p03-030>, <http://www.nrcresearchpress.com/doi/10.1139/p03-030>, 2003.

Barnes, P. R., Wolff, E. W., Mallard, D. C., and Mader, H. M.: SEM studies of the morphology and chemistry of polar ice, *Microscopy Research and Technique*, 62, 62–69, <https://doi.org/10.1002/jemt.10385>, 2003a.

Barnes, P. R. F. and Wolff, E. W.: Distribution of soluble impurities in cold glacial ice, *Journal of Glaciology*, 50, 311–324, <https://doi.org/10.3189/172756504781829918>, 2004.

665 Barnes, P. R. F., Mulvaney, R., Robinson, K., and Wolff, E. W.: Observations of polar ice from the Holocene and the glacial period using the scanning electron microscope, *Annals of Glaciology*, 35, 559–566, 2002.

Barnes, P. R. F., Wolff, E. W., Mader, H. M., Udisti, R., Castellano, E., and Röthlisberger, R.: Evolution of chemical peak shapes in the Dome C, Antarctica, ice core, *Journal of Geophysical Research*, 108, 4126, <https://doi.org/10.1029/2002JD002538>, 2003b.

Bartels-Rausch, T., Jacobi, H.-W., Kahan, T. F., Thomas, J. L., Thomson, E. S., Abbatt, J. P. D., Ammann, M., Blackford, J. R., Bluhm, 670 H., Boxe, C., Domine, F., Frey, M. M., Gladich, I., Guzmán, M. I., Heger, D., Huthwelker, T., Klán, P., Kuhs, W. F., Kuo, M. H., Maus, S., Moussa, S. G., McNeill, V. F., Newberg, J. T., Pettersson, J. B. C., Roeselová, M., and Sodeau, J. R.: A review of air–ice chemical and physical interactions (AICI): liquids, quasi-liquids, and solids in snow, *Atmospheric Chemistry and Physics*, 14, 1587–1633, <https://doi.org/10.5194/acp-14-1587-2014>, 2014.

Bohleber, P., Roman, M., Šala, M., and Barbante, C.: Imaging the impurity distribution in glacier ice cores with LA-ICP-MS, *Journal of 675 Analytical Atomic Spectrometry*, <https://doi.org/10.1039/d0ja00170h>, 2020.

Bory, A. J.-M., Biscaye, P. E., Piotrowski, A. M., and Steffensen, J. P.: Regional variability of ice core dust composition and provenance in Greenland, *Geochemistry, Geophysics, Geosystems*, 4, 1–8, <https://doi.org/10.1029/2003GC000627>, 2003.

Cole-Dai, J., Budner, D. M., and Ferris, D. G.: High Speed, High Resolution, and Continuous Chemical Analysis of Ice Cores Using a Melter and Ion Chromatography, *Environmental Science & Technology*, 40, 6764–6769, <https://doi.org/10.1021/es061188a>, 2006.

680 Dahl-Jensen, D. and Gundestrup, N. S.: Constitutive properties of ice at Dye 3, Greenland, International Association of Hydrological Sciences Publication, pp. 31–43, [http://hydrologie.org/redbooks/a170/iahs\\_170\\_0031.pdf](http://hydrologie.org/redbooks/a170/iahs_170_0031.pdf), 1987.

Dahl-Jensen, D., Albert, M. R., Aldahan, A., Azuma, N., Balslev-Clausen, D., Baumgartner, M., Berggren, A. M., Bigler, M., Binder, T., Blunier, T., Bourgeois, J. C., Brook, E. J., Buchardt, S. L., Buizert, C., Capron, E., Chappellaz, J., Chung, J., Clausen, H. B., Cvijanovic, I., Davies, S. M., Ditlevsen, P., Eicher, O., Fischer, H., Fisher, D. A., Fleet, L. G., Gfeller, G., Gkinis, V., Gogineni, S., Goto-Azuma, K., Grinsted, A., Gudlaugsdottir, H., Guillevic, M., Hansen, S. B., Hansson, M., Hirabayashi, M., Hong, S., Hur, S. D., Huybrechts, P., Hvidberg, C. S., Iizuka, Y., Jenk, T., Johnsen, S. J., Jones, T. R., Jouzel, J., Karlsson, N. B., Kawamura, K., Keegan, K., Kettner, E., Kipfstuhl, S., Kjær, H. A., Koutnik, M., Kuramoto, T., Köhler, P., Laepple, T., Landais, A., Langen, P. L., Larsen, L. B., Leuenberger, D., Leuenberger, M., Leuschen, C., Li, J., Lipenkov, V., Martinerie, P., Maselli, O. J., Masson-Delmotte, V., McConnell, J. R., Miller, H., Mini, O., Miyamoto, A., Montagnat-Rentier, M., Mulvaney, R., Muscheler, R., Orsi, A. J., Paden, J., Panton, C., Pattyn, F., Petit, J. R., 685 Pol, K., Popp, T., Possnert, G., Prié, F., Prokopiou, M., Quiquet, A., Rasmussen, S. O., Raynaud, D., Ren, J., Reutenauer, C., Ritz, C., Röckmann, T., Rosen, J. L., Rubino, M., Rybak, O., Samyn, D., Sapart, C. J., Schilt, A., Schmidt, A. M., Schwander, J., Schüpbach, S., Seierstad, I., Severinghaus, J. P., Sheldon, S., Simonsen, S. B., Sjolte, J., Solgaard, A. M., Sowers, T., Sperlich, P., Steen-Larsen, H. C., Steffen, K., Steffensen, J. P., Steinhage, D., Stocker, T. F., Stowasser, C., Sturevik, A. S., Sturges, W. T., Sveinbjörnsdóttir, A., Svensson, A., Tison, J. L., Uetake, J., Valletonga, P., Van De Wal, R. S., Van Der Wel, G., Vaughn, B. H., Vinther, B., Waddington, E., Wegner, A., 690 Weikusat, I., White, J. W., Wilhelms, F., Winstrup, M., Witrant, E., Wolff, E. W., Xiao, C., and Zheng, J.: Eemian interglacial reconstructed from a Greenland folded ice core, *Nature*, 493, 489–494, <https://doi.org/10.1038/nature11789>, 2013.

de Angelis, M., Tison, J. L., Morel-Fourcade, M. C., and Susini, J.: Micro-investigation of EPICA Dome C bottom ice: Evidence of long term in situ processes involving acid-salt interactions, mineral dust, and organic matter, *Quaternary Science Reviews*, 78, 248–265, <https://doi.org/10.1016/j.quascirev.2013.08.012>, 2013.

700 Della Lunga, D., Müller, W., Rasmussen, S. O., and Svensson, A.: Location of cation impurities in NGRIP deep ice revealed by cryo-cell UV-laser-ablation ICPMS, *Journal of Glaciology*, 60, 970–988, <https://doi.org/10.3189/2014JoG13J199>, 2014.

Eichler, J., Kleitz, I., Bayer-Giraldi, M., Jansen, D., Kipfstuhl, S., Shigeyama, W., Weikusat, C., and Weikusat, I.: Location and distribution of micro-inclusions in the EDML and NEEM ice cores using optical microscopy and in situ Raman spectroscopy, *Cryosphere*, 11, 1075–1090, <https://doi.org/10.5194/tc-11-1075-2017>, 2017.

705 Eichler, J., Weikusat, C., Wegner, A., Twarloh, B., Behrens, M., Fischer, H., Hörhold, M., Jansen, D., Kipfstuhl, S., Ruth, U., Wilhelms, F., and Weikusat, I.: Impurity Analysis and Microstructure Along the Climatic Transition From MIS 6 Into 5e in the EDML Ice Core Using Cryo-Raman Microscopy, *Frontiers in Earth Science*, 7, 1–16, <https://doi.org/10.3389/feart.2019.00020>, 2019.

EPICA Community Members: Eight glacial cycles from an Antarctic ice core EPICA community members, *Nature*, 429, 623–628, 2004.

Erhardt, T., Jensen, C. M., Borovinskaya, O., and Fischer, H.: Single Particle Characterization and Total Elemental Concentration Measurements in Polar Ice Using Continuous Flow Analysis-Inductively Coupled Plasma Time-of-Flight Mass Spectrometry, *Environmental Science & Technology*, 53, 13 275–13 283, <https://doi.org/10.1021/acs.est.9b03886>, 2019.

710 Faria, S. H., Freitag, J., and Kipfstuhl, S.: Polar ice structure and the integrity of ice-core paleoclimate records, *Quaternary Science Reviews*, 29, 338–351, <https://doi.org/10.1016/j.quascirev.2009.10.016>, 2010.

Faria, S. H., Weikusat, I., and Azuma, N.: The microstructure of polar ice. Part II: State of the art, *Journal of Structural Geology*, 61, 21–49, 715 <https://doi.org/10.1016/j.jsg.2013.11.003>, 2014.

Fitzpatrick, J. J., Voigt, D. E., Fegyveresi, J. M., Stevens, N. T., Spencer, M. K., Cole-Dai, J., Alley, R. B., Jardine, G. E., Cravens, E. D., Wilen, L. A., Fudge, T., and McConnell, J. R.: Physical properties of the WAIS Divide ice core, *Journal of Glaciology*, 60, 1181–1198, <https://doi.org/10.3189/2014JoG14J100>, 2014.

Fukazawa, H., Suzuki, D., Ikeda, T., Mae, S., and Hondoh, T.: Raman Spectra of Translational Lattice Vibrations in Polar Ice, *The Journal of Physical Chemistry B*, 101, 6184–6187, <https://doi.org/10.1021/jp963161r>, 1997.

Fukazawa, H., Sugiyama, K., Shinji, M., Narita, H., and Hondoh, T.: Acid ions at triple junction of Antarctic ice observed by Raman scattering, *Geophysical Research Letters*, 25, 2845–2848, 1998.

Gerber, T. A., Hvidberg, C. S., Rasmussen, S. O., Franke, S., Sinnl, G., Grinsted, A., Jansen, D., and Dahl-Jensen, D.: Upstream flow effects revealed in the EastGRIP ice core using Monte Carlo inversion of a two-dimensional ice-flow model, *The Cryosphere*, 15, 3655–3679, 725 <https://doi.org/10.5194/tc-15-3655-2021>, 2021.

Glen, J. W.: The Effect of Hydrogen Disorder on Dislocation Movement and Plastic Deformation of Ice, *Physik der kondensierten Materie*, 7, 43–51, 1968.

Han, C., Do Hur, S., Han, Y., Lee, K., Hong, S., Erhardt, T., Fischer, H., Svensson, A. M., Steffensen, J. P., and Valletlonga, P.: High-resolution isotopic evidence for a potential Saharan provenance of Greenland glacial dust, *Scientific Reports*, 8, 15 582, 730 <https://doi.org/10.1038/s41598-018-33859-0>, 2018.

Hörhold, M. W., Laepple, T., Freitag, J., Bigler, M., Fischer, H., and Kipfstuhl, S.: On the impact of impurities on the densification of polar firn, *Earth and Planetary Science Letters*, 325–326, 93–99, <https://doi.org/10.1016/j.epsl.2011.12.022>, 2012.

Hu, X., Jia, K., Liu, F., Baker, I., and Black, D.: Dislocation Mobility in HCL-doped Ice, *Proceedings of the Material Research Society*, 375, 287–292, 1995.

Humphreys, F. and Hatherly, M.: *Recrystallization and Related Annealing Phenomena*, Elsevier, <https://doi.org/10.1016/B978-0-08-044164-1.X5000-2>, 2004.

Hvidberg, C. S., Grinsted, A., Dahl-Jensen, D., Khan, S. A., Kusk, A., Andersen, J. K., Neckel, N., Solgaard, A., Karlsson, N. B., Kjær, H. A., and Valletlonga, P.: Surface velocity of the Northeast Greenland Ice Stream (NEGIS): assessment of interior velocities derived from satellite data by GPS, *The Cryosphere*, 14, 3487–3502, <https://doi.org/10.5194/tc-14-3487-2020>, 2020.

Iizuka, Y., Horikawa, S., Sakurai, T., Johnson, S., Dahl-Jensen, D., Steffensen, J. P., and Hondoh, T.: A relationship between ion balance and the chemical compounds of salt inclusions found in the Greenland Ice Core Project and Dome Fuji ice cores, *Journal of Geophysical Research Atmospheres*, 113, 1–11, <https://doi.org/10.1029/2007JD009018>, 2008.

Iizuka, Y., Tsuchimoto, A., Hoshina, Y., Sakurai, T., Hansson, M., Karlin, T., Fujita, K., Nakazawa, F., Motoyama, H., and Fujita, S.: The rates of sea salt sulfatization in the atmosphere and surface snow of inland Antarctica, *Journal of Geophysical Research: Atmospheres*, 745 117, <https://doi.org/10.1029/2011JD016378>, 2012.

Iliescu, D. and Baker, I.: Effects of impurities and their redistribution during recrystallization of ice crystals, *Journal of Glaciology*, 54, 362–370, 2008.

Jones, S. J. and Glen, J. W.: The effect of dissolved impurities on the mechanical properties of ice crystals, *Philosophical Magazine*, 19, 13–24, <https://doi.org/10.1080/14786436908217758>, 1969.

Joughin, I., Smith, B. E., Howat, I. M., Scambos, T., and Moon, T.: Greenland flow variability from ice-sheet-wide velocity mapping, *Journal of Glaciology*, 56, 415–430, <https://doi.org/10.3189/002214310792447734>, 2010.

Kaufmann, P. R., Federer, U., Hutterli, M. A., Bigler, M., Schüpbach, S., Ruth, U., Schmitt, J., and Stocker, T. F.: An Improved Continuous Flow Analysis System for High-Resolution Field Measurements on Ice Cores, *Environmental Science & Technology*, 42, 8044–8050, <https://doi.org/10.1021/es8007722>, 2008.

755 755 Kerminen, V.-M., Teinilä, K., and Hillamo, R.: Chemistry of sea-salt particles in the summer Antarctic atmosphere, *Atmospheric Environment*, 34, 2817–2825, [https://doi.org/10.1016/S1352-2310\(00\)00089-3](https://doi.org/10.1016/S1352-2310(00)00089-3), 2000.

Kipfstuhl, Sepp, Hamann, Ilka, Lambrecht, Anja, Freitag, Johannes, Faria, Sergio, H., Grigoriev, Dimitri, Azuma, and Nobuhiko: Microstructure mapping: a new method for imaging deformation-induced microstructural features of ice on the grain scale, *Journal of Glaciology*, 52, 398–406, 2006.

760 760 Lafuente, B., Downs, R. T., Yang, H., and Stone, N.: 1. The power of databases: The RRUFF project, in: *Highlights in Mineralogical Crystallography*, edited by Armbruster, T. and Danisi, R. M., pp. 1–30, De Gruyter, Berlin, <https://doi.org/10.1515/9783110417104-003>, 2015.

Lecavalier, B. S., Milne, G. A., Simpson, M. J., Wake, L., Huybrechts, P., Tarasov, L., Kjeldsen, K. K., Funder, S., Long, A. J., Woodroffe, S., Dyke, A. S., and Larsen, N. K.: A model of Greenland ice sheet deglaciation constrained by observations of relative sea level and ice extent, *Quaternary Science Reviews*, 102, 54–84, <https://doi.org/10.1016/j.quascirev.2014.07.018>, 2014.

765 Legrand, M. and Mayewski, P.: Glaciochemistry of polar ice cores: A review, *Reviews of Geophysics*, 35, 219–243, <https://doi.org/10.1029/96RG03527>, 1997.

Legrand, M. R. and Delmas, R. J.: Soluble Impurities in Four Antarctic Ice Cores Over the Last 30 000 Years, *Annals of Glaciology*, 10, 116–120, <https://doi.org/10.3189/s026030550004274>, 1988.

770 770 Masson-Delmotte, V., Stenni, B., Pol, K., Braconnot, P., Cattani, O., Falourd, S., Kageyama, M., Jouzel, J., Landais, A., Minster, B., Barnola, J. M., Chappellaz, J., Krinner, G., Johnsen, S., Röhlisberger, R., Hansen, J., Mikolajewicz, U., and Otto-Bliesner, B.: EPICA Dome C record of glacial and interglacial intensities, *Quaternary Science Reviews*, 29, 113–128, <https://doi.org/10.1016/j.quascirev.2009.09.030>, 2010.

McConnell, J. R., Lamorey, G. W., Lambert, S. W., and Taylor, K. C.: Continuous Ice-Core Chemical Analyses Using Inductively Coupled 775 Plasma Mass Spectrometry, *Environmental Science & Technology*, 36, 7–11, <https://doi.org/10.1021/es011088z>, 2002.

Miyamoto, A., Narita, H., Hondoh, T., Shoji, H., Kawada, K., Watanabe, O., Dahl-Jensen, D., Gundestrup, N. S., Clausen, H. B., and Duval, P.: Ice-sheet flow conditions deduced from mechanical tests of ice core, in: *Annals of Glaciology*, vol. 29, pp. 179–183, <https://doi.org/10.3189/172756499781820950>, 1999.

780 780 Mojtabavi, S., Wilhelms, F., Cook, E., Davies, S. M., Sinnl, G., Skov Jensen, M., Dahl-Jensen, D., Svensson, A., Vinther, B. M., Kipfstuhl, S., Jones, G., Karlsson, N. B., Faria, S. H., Gkinis, V., Kjær, H. A., Erhardt, T., Berben, S. M. P., Nisancioglu, K. H., Koldtoft, I., and Rasmussen, S. O.: A first chronology for the East Greenland Ice-core Project (EGRIP) over the Holocene and last glacial termination, *Climate of the Past*, 16, 2359–2380, <https://doi.org/10.5194/cp-16-2359-2020>, 2020a.

Mojtabavi, S., Wilhelms, F., Cook, E., Davies, S. M., Sinnl, G., Skov Jensen, M., Dahl-Jensen, D., Svensson, A. M., Møllesø Vinther, B., Kipfstuhl, S., Karlsson, N. B., Faria, S. H., Gkinis, V., Kjær, H. A., Erhardt, T., Berben, S. M. P., Nisancioglu, K. H., Koldtoft, I., and Rasmussen, S. O.: Acidity measured with the Electrical Conductivity Method (ECM) on the EGRIP ice core (down to 1383.84 m depth), converted to hydrogen ion concentration, <https://doi.org/10.1594/PANGAEA.922199>, <https://doi.org/10.1594/PANGAEA.922199>, 2020b.

Mojtabavi, S., Wilhelms, F., Cook, E., Davies, S. M., Sinnl, G., Skov Jensen, M., Dahl-Jensen, D., Svensson, A. M., Møllesø Vinther, B., Kipfstuhl, S., Karlsson, N. B., Faria, S. H., Gkinis, V., Kjær, H. A., Erhardt, T., Berben, S. M. P., Nisancioglu, K. H., Koldtoft, I., and

790 Rasmussen, S. O.: Specific conductivity measured with the dielectric profiling (DEP) technique on the EGRIP ice core, 13.77-1383.84 m depth, <https://doi.org/10.1594/PANGAEA.919313>, <https://doi.org/10.1594/PANGAEA.919313>, 2020c.

Nakazawa, F., Nagatsuka, N., Hirabayashi, M., Goto-Azuma, K., Steffensen, J. P., and Dahl-Jensen, D.: Variation in recent annual snow deposition and seasonality of snow chemistry at the east Greenland ice core project (EGRIP) camp, Greenland, *Polar Science*, 27, 100597, <https://doi.org/10.1016/j.polar.2020.100597>, 2021.

795 Neff, P. D.: A review of the brittle ice zone in polar ice cores, *Annals of Glaciology*, 55, 72–82, <https://doi.org/10.3189/2014AoG68A023>, 2014.

Ng, F. S. L.: Pervasive diffusion of climate signals recorded in ice-vein ionic impurities, *The Cryosphere*, 15, 1787–1810, <https://doi.org/10.5194/tc-15-1787-2021>, 2021.

Obbard, R. and Baker, I.: The microstructure of meteoric ice from Vostok, Antarctica, *Journal of Glaciology*, 53, 41–62, 2007.

800 Ohno, H., Lipenkov, V. Y., and Hondoh, T.: Air bubble to clathrate hydrate transformation in polar ice sheets: A reconsideration based on the new data from Dome Fuji ice core, *Geophysical Research Letters*, 31, <https://doi.org/10.1029/2004GL021151>, 2004.

Ohno, H., Igarashi, M., and Hondoh, T.: Salt inclusions in polar ice core: Location and chemical form of water-soluble impurities, *Earth and Planetary Science Letters*, 232, 171–178, <https://doi.org/10.1016/j.epsl.2005.01.001>, 2005.

805 Ohno, H., Igarashi, M., and Hondoh, T.: Characteristics of salt inclusions in polar ice from Dome Fuji, East Antarctica, *Geophysical Research Letters*, 33, L08501, <https://doi.org/10.1029/2006GL025774>, 2006.

Ohno, H., Lipenkov, V. Y., and Hondoh, T.: Formation of air clathrate hydrates in polar ice sheets: heterogeneous nucleation induced by micro-inclusions, *Journal of Glaciology*, 56, 917–921, <https://doi.org/10.3189/002214310794457317>, 2010.

810 Ohno, H., Iizuka, Y., Horikawa, S., Sakurai, T., Hondoh, T., and Motoyama, H.: Potassium alum and aluminum sulfate micro-inclusions in polar ice from Dome Fuji, East Antarctica, *Polar Science*, 8, 1–9, <https://doi.org/10.1016/j.polar.2013.11.003>, 2014.

Paterson, W. S. B.: Why ice-age ice is sometimes "soft", *Cold Regions Science and Technology*, 20, 75–98, 1991.

815 Petit, J. R., Duval, P., and Lorius, C.: Long-term climatic changes indicated by crystal growth in polar ice, *Nature*, 326, 62–64, 1987.

Petrenko, V. F. and Whitworth, R. W.: *Physics of ice*, Clarendon Press, London, 1999.

Raman, C. V. and Krishnan, K. S.: A New Type of Secondary Radiation, *Nature*, 121, 501–502, 1928.

820 Reinhardt, H., Kriews, M., Miller, H., Schrems, O., Lüdke, C., Hoffmann, E., and Skole, J.: Laser ablation inductively coupled plasma mass spectrometry: a new tool for trace element analysis in ice cores, *Fresenius' Journal of Analytical Chemistry*, 370, 629–636, <https://doi.org/10.1007/s002160100853>, 2001.

Röthlisberger, R.: Limited dechlorination of sea-salt aerosols during the last glacial period: Evidence from the European Project for Ice Coring in Antarctica (EPICA) Dome C ice core, *Journal of Geophysical Research*, 108, 4526, <https://doi.org/10.1029/2003JD003604>, 2003.

Röthlisberger, R., Bigler, M., Hutterli, M., Sommer, S., Stauffer, B., Junghans, H. G., and Wagenbach, D.: Technique for continuous high-resolution analysis of trace substances in firn and ice cores, *Environmental Science and Technology*, 34, 338–342, <https://doi.org/10.1021/es9907055>, 2000a.

Röthlisberger, R., Hutterli, M. A., Sommer, S., Wolff, E. W., and Mulvaney, R.: Factors controlling nitrate in ice cores: Evidence from the Dome C deep ice core, *Journal of Geophysical Research Atmospheres*, 105, 20565–20572, <https://doi.org/10.1029/2000JD900264>, 2000b.

825 Ruth, U., Wagenbach, D., Steffensen, J. P., and Bigler, M.: Continuous record of microparticle concentration and size distribution in the central Greenland NGRIP ice core during the last glacial period, *Journal of Geophysical Research: Atmospheres*, 108, <https://doi.org/10.1029/2002JD002376>, 2003.

Sakurai, T., Ilzuka, Y., Horikawa, S., Johnsen, S., Dahl-Jensen, D., Steffensen, J. P., and Hondoh, T.: Direct observation of salts as micro-inclusions in the Greenland GRIP ice core, *Journal of Glaciology*, 55, 777–783, <https://doi.org/10.3189/002214309790152483>, 2009.

830 Sakurai, T., Ohno, H., Genceli, F. E., Horikawa, S., Iizuka, Y., Uchida, T., and Hondoh, T.: Magnesium methanesulfonate salt found in the Dome Fuji (Antarctica) ice core, *Journal of Glaciology*, 56, 837–842, <https://doi.org/10.3189/002214310794457335>, 2010.

Sakurai, T., Ohno, H., Horikawa, S., Iizuka, Y., Uchida, T., Hirakawa, K., and Hondoh, T.: The chemical forms of water-soluble microparticles preserved in the Antarctic ice sheet during Termination I, *Journal of Glaciology*, 57, 1027–1032, <https://doi.org/10.3189/002214311798843403>, 2011.

835 Simonsen, M. F., Baccolo, G., Blunier, T., Borunda, A., Delmonte, B., Frei, R., Goldstein, S., Grinsted, A., Kjær, H. A., Sowers, T., Svensson, A., Vinther, B., Vladimirova, D., Winckler, G., Winstrup, M., and Vallelonga, P.: East Greenland ice core dust record reveals timing of Greenland ice sheet advance and retreat, *Nature Communications*, 10, <https://doi.org/10.1038/s41467-019-12546-2>, <http://dx.doi.org/10.1038/s41467-019-12546-2>, 2019.

Smith, C. S.: Grains, phases, and interfaces: An introduction of microstructure, *Trans. AIME*, 175, 15–51, 1948.

840 Steffensen, J. P.: The size distribution of microparticles from selected segments of the Greenland Ice Core Project ice core representing different climatic periods, *Journal of Geophysical Research*, 102, 755–2, 1997.

Steffensen, J. P., Andersen, K. K., Bigler, M., Clausen, H. B., Dahl-Jensen, D., Fischer, H., Goto-Azuma, K., Hansson, M., Johnsen, S. J., Jouzel, J., Masson-Delmotte, V., Popp, T., Rasmussen, S. O., Rothlisberger, R., Ruth, U., Stauffer, B., Siggaard-Andersen, M.-L., Sveinbjornsdottir, A. E., Svensson, A., and White, J. W. C.: High-Resolution Greenland Ice Core Data Show Abrupt Climate Change Happens in Few Years, *Science*, 321, 680–684, <https://doi.org/10.1126/science.1157707>, 2008.

845 Stoll, N., Eichler, J., Hörhold, M., Erhardt, T., Jensen, C., and Weikusat, I.: Microstructure, Micro-inclusions and Mineralogy along the EGRIP ice core - Part 1: Localisation of inclusions and deformation patterns, *The Cryosphere Discussions*, pp. 1–29, <https://doi.org/https://doi.org/10.5194/tc-2021-188>, 2021a.

Stoll, N., Eichler, J., Hörhold, M., Shigeyama, W., and Weikusat, I.: A Review of the Microstructural Location of Impurities and Their Impacts on Deformation, *Frontiers in Earth Science*, 8, <https://doi.org/10.3389/feart.2020.615613>, 2021b.

850 Svensson, A., Biscaye, P. E., and Grousset, F. E.: Characterization of late glacial continental dust in the Greenland Ice Core Project ice core, *Journal of Geophysical Research: Atmospheres*, 105, 4637–4656, <https://doi.org/10.1029/1999JD901093>, 2000.

Svensson, A., Nielsen, S. W., Kipfstuhl, S., Johnsen, S. J., Steffensen, J. P., Bigler, M., Ruth, U., and Röthlisberger, R.: Visual stratigraphy of the North Greenland Ice Core Project (NorthGRIP) ice core during the last glacial period, *Journal of Geophysical Research*, 110, 1–11, <https://doi.org/10.1029/2004JD005134>, 2005.

855 Syring, N., Stein, R., Fahl, K., Vahlenkamp, M., Zehnich, M., Spielhagen, R. F., and Niessen, F.: Holocene changes in sea-ice cover and polynya formation along the eastern North Greenland shelf: New insights from biomarker records, *Quaternary Science Reviews*, 231, 106 173, <https://doi.org/10.1016/j.quascirev.2020.106173>, 2020.

Thorsteinsson, T., Kipfstuhl, J., and Miller, H.: Textures and fabrics in the GRIP ice core, *Journal of Geophysical Research: Oceans*, 102, 26 583–26 599, <https://doi.org/10.1029/97JC00161>, 1997.

860 Vallelonga, P. and Svensson, A.: Ice Core Archives of Mineral Dust, in: *Mineral Dust*, pp. 463–485, Springer Netherlands, Dordrecht, [https://doi.org/10.1007/978-94-017-8978-3\\_18](https://doi.org/10.1007/978-94-017-8978-3_18), 2014.

Vallelonga, P., Christianson, K., Alley, R. B., Anandakrishnan, S., Christian, J. E., Dahl-Jensen, D., Gkinis, V., Holme, C., Jacobel, R. W., Karlsson, N. B., Keisling, B. A., Kipfstuhl, S., Kjær, H. A., Kristensen, M. E., Muto, A., Peters, L. E., Popp, T., Riverman, K. L., Svensson, A. M., Tibuleac, C., Vinther, B. M., Weng, Y., and Winstrup, M.: Initial results from geophysical surveys and shallow coring of the Northeast Greenland Ice Stream (NEGIS), *Cryosphere*, 8, 1275–1287, <https://doi.org/10.5194/tc-8-1275-2014>, 2014.

865 Walker, M., Head, M. J., Berkelhammer, M., Björck, S., Cheng, H., Cwynar, L., Fisher, D., Gkinis, V., Long, A., Lowe, J., Newnham, R., Rasmussen, S. O., and Weiss, H.: Formal ratification of the subdivision of the Holocene Series/Epoch (Quaternary System/Period): two new Global Boundary Stratotype Sections and Points (GSSPs) and three new stages/subseries, *Episodes*, 41, 213–223, 870 <https://doi.org/10.18814/epiugs/2018/018016>, 2018.

Weertman, J. and Weertman, J. R.: *Elementary Dislocation Theory*, Oxford University Press, Oxford, 1992.

Wegner, A., Fischer, H., Delmonte, B., Petit, J.-R., Erhardt, T., Ruth, U., Svensson, A., Vinther, B., and Miller, H.: The role of seasonality of mineral dust concentration and size on glacial/interglacial dust changes in the EPICA Dronning Maud Land ice core, *Journal of Geophysical Research: Atmospheres*, 120, 9916–9931, <https://doi.org/10.1002/2015JD023608>, 2015.

875 Weikusat, C., Freitag, J., and Kipfstuhl, S.: Raman spectroscopy of gaseous inclusions in EDML ice core: first results – microbubbles, *Journal of Glaciology*, 58, 761–766, <https://doi.org/10.3189/2012JoG11J222>, 2012.

Weikusat, C., Kipfstuhl, S., and Weikusat, I.: Raman tomography of natural air hydrates, *Journal of Glaciology*, 61, 923–930, <https://doi.org/10.3189/2015JoG15J009>, 2015.

Weikusat, I., Westhoff, J., Kipfstuhl, S., and Jansen, D.: Visual stratigraphy of the EastGRIP ice core (14 m - 2021 m depth, drilling period 880 2017-2019), <https://doi.org/10.1594/PANGAEA.925014>, <https://doi.org/10.1594/PANGAEA.925014>, 2020.

Weiss, J., Vidot, J., Gay, M., Arnaud, L., Duval, P., and Petit, J. R.: Dome Concordia ice microstructure: impurities effect on grain growth, *Annals of Glaciology*, 35, 552–558, <https://doi.org/10.3189/172756402781816573>, 2002.

Westhoff, J., Stoll, N., Franke, S., Weikusat, I., Bons, P., Kerch, J., Jansen, D., Kipfstuhl, S., and Dahl-Jensen, D.: A stratigraphy-based method for reconstructing ice core orientation, *Annals of Glaciology*, pp. 1–12, <https://doi.org/10.1017/aog.2020.76>, 2020.

885 Wilhelms, F., Kipfstuhl, J., Miller, H., Heinloth, K., and Firestone, J.: Precise dielectric profiling of ice cores: a new device with improved guarding and its theory, *Journal of Glaciology*, 44, 171–174, 1998.

Wolff, E. W., Mulvaney, R., and Oatest, K.: The location of impurities in Antarctic ice, *Annals of Glaciology*, 11, 194–197, 1988.

Wolff, E. W., Miners, W. D., Moore, J. C., and Paren, J. G.: Factors Controlling the Electrical Conductivity of Ice from the Polar Regions-A Summary, *The Journal of Physical Chemistry B*, 101, 6090–6094, <https://doi.org/10.1021/jp9631543>, 1997.

890 Young, N. E. and Briner, J. P.: Holocene evolution of the western Greenland Ice Sheet: Assessing geophysical ice-sheet models with geological reconstructions of ice-margin change, *Quaternary Science Reviews*, 114, 1–17, <https://doi.org/10.1016/j.quascirev.2015.01.018>, 2015.